Structural Analysis of the Electron Transfer Complex Between Ferredoxin–Thioredoxin Reductase and Thioredoxin

（フェレドキシン–チオレドキシン還元酵素とチオレドキシンが形成する電子伝達複合体の構造研究）

Linda Juniar

A dissertation submitted to

Department of Biological Science

Graduate School of Science

Osaka University

Japan

2020

ACKNOWLEDGMENTS

The author wishes to express sincere appreciation to my advisor Prof. Genji Kurisu for the continuous support of my Ph.D. study and other related projects for his patience, motivation, and immense knowledge. His guidance helped me in all the time of research and writing of this dissertation. Further, I would like to extend my deepest gratitude to Dr. Hideaki Tanaka for his valuable advice, practical suggestions, and insight into protein structure analysis.

I would like to thank my collaborator at Tokyo Institute of Technology, Prof. Toru Hisabori and Dr. Keisuke Yoshida for their kind help and support. I would like to extend my thanks to the rest of my dissertation committee: Prof. Toshimichi Fujiwara and Dr. Hirozo Oh-oka for the thoughtful comments and suggestions on this dissertation. I thank to Dr. Ju Yaen Kim for her help in the initial sample preparation. I am also grateful to Dr. Eiki Yamashita for his kind advice and support in SPring-8.

Special thanks to the members of Protein Crystallography Laboratory for their support, the illuminating discussions, and all the fun we had in the last three years. To conclude, I cannot forget to thank my family and friends for all unconditional support in this very intense academic year.

ABSTRACT

Plants have developed regulatory systems to survive through fluctuating light environments. For optimization of metabolic flux in the stroma under such condition, chloroplasts have to tune their metabolic reactions in a light-dependent manner. Thiol-based redox regulation is one of the mechanisms developed to control the enzymatic reactions in chloroplast. In this system, two soluble redox-mediator proteins, known as ferredoxin–thioredoxin reductase (FTR) and thioredoxin (Trx), sequentially transfer the electron from the photosynthetic electron transport chain to the target enzymes such as fructose 1,6-bisphosphatase, NADP-malate dehydrogenase or 2-Cys peroxiredoxins.

Completion of *Arabidopsis thaliana* genome sequencing has indicated that 10 Trx isoforms are localized in chloroplasts and classified into five subtypes (two Trx-*f*, four Trx-*m*, one Trx-*x*, two Trx-*y*, and one Trx-*z*). On the other hand, the catalytic subunit of FTR is encoded by a unique gene associated with a variable subunit encoded by two genes. FTR acts as an important protein that transfers reducing equivalents from the photosynthetic electron transport chain to Trxs. Several structures of Trxs have been determined by X-ray crystallography. Despite the common Trx-fold, each Trx shows different molecular characteristics, such as the protein surface charge and midpoint redox potential (E_m), leading to their differences in target and protein-protein interaction. Based on their FTR-dependent kinetic parameters, *A. thaliana* Trxs can be clustered into three classes: high, middle, and low efficiency group. The comparative kinetic analysis showed that the electron transfer efficiency from FTR to Trx is not fully controlled by E_m but also by other factors. To date, the three-dimensional structure of *Synechocystis* FTR and spinach Trx complexes

have been reported. The interaction of Trx-*m* with FTR is similar to that of Trx-*f*. The conformational difference exists in small rotation angles of Trx molecule to the flat FTR molecule. Since this published FTR:Trx complex consisted of proteins from different organisms, I could not refer those non-physiological complex structures to explain the differences in FTR affinity to three classes of Trx from *A. thaliana*. Therefore, I focused on the physiological complex between FTR and Trx isoforms from *A. thaliana*. After extensive screening of crystallization, I have chosen Trx-*y*1, Trx-*f*2 and Trx-*m*2 as a representative for high, middle and low efficiency group, respectively.

In this research, I have successfully determined three structures of FTR:Trx protein complex; FTR:Trx-*y*1; FTR:Trx-*f*2; and FTR:Trx-*m*2, at 1.59 Å, 1.79 Å and 2.4 Å, respectively. FTR:Trx-*f*2 and FTR:Trx-*m*2 complexes contained Trx, catalytic and variable subunit of FTR, whereas FTR:Trx-*y*1 contained Trx and FTR catalytic subunit only. The overall structure of three FTR:Trx complexes was similar with the rmsd values of 0.588 Å based on the Cα atoms of FTR, and the values ranging from 1.2 to 1.5 Å based on those of Trxs. Trx molecules interacted mostly with catalytic subunit of FTR with different rotational angles of 7.9-16.1 degree in polar angle of kappa.

I performed superposition of FTR and Trx in the complex and single form to study the structural changes upon complex formation. I used *Synechosystis* FTR structure (PDB ID 1DJ7) for comparison with *A. thaliana* FTR in FTR:Trx complexes, and *A. thaliana* Trx-*m*1 (determined at 1.1 Å resolution) and spinach Trx-*f* (PDB ID 1FAA) for comparison with Trx in the complexes. Since there are no available structures of Trx-*y* monomer, I could not do the same analysis for Trx-*y*1. The structural comparison results showed that there were microscopic changes of FTR or Trx upon complex formation. The

biggest structural differences were found in the side chain conformations located at the molecular interface.

Since the resolution of the complex structures were quite good, I comparatively studied the interaction between FTR and Trxs. The Trx molecules interact with FTR mainly through hydrophobic interactions which can be clustered into two types, common interaction for all Trx isoforms and isoform-specific peripheral interaction. The FTR:Trx-*y*1 complex had more isoform-specific interactions, followed by FTR:Trx-*f*2 and FTR:Trx-*m*2, which was supported by the total buried surface area of FTR:Trx-*y*1 around 1622 $Å^2$ whereas Trx-*f*2 and Trx-*m*2 were 1470 $Å^2$, and 1509 $Å^2$, respectively. $S_{0.5}$ of Trx-*y*1 was 10-fold smaller than that of Trx-*f*2, while $S_{0.5}$ of Trx-*m*2 was not so different from that of Trx-*f*2. The electrostatic potential of each Trx may drive the differences in isoform-specific interaction leading to different affinity of FTR toward Trx.

Based on my determined three X-ray structures of FTR:Trxs, I have concluded that there were small but significant structural changes of FTR and Trx upon complex formation, and the number of isoform-specific interaction located peripherally is the key for the three classes of enzymatic efficiency, which may be facilitated by the differential charged surface of Trx isoforms.

TABLE OF CONTENTS

ABBREVIATION

ADP	Adenosine diphosphate
ATP	Adenosine triphosphate
$Cytb_6f$	Cytochrome b_6f
DTT	Dithiothreitol
EDTA	Ethylenediaminetetraacetic acid
FBPase	Fructose 1,6-bisphosphatase
Fd	Ferredoxin
FNR	Ferredoxin–$NADP^+$ reductase
FTR	Ferredoxin–thioredoxin reductase
FTRC	Catalytic subunit of FTR
FTRC	Variable subunit of FTR
ssFTR	*Synechocystis sp.* FTR
atFTR	*Arabidopsis thaliana* FTR
IPTG	Isopropyl-1-thio-β-D-galactopyranoside
LB	Luria-bertani
NADPH	Nicotinamide adenine dinucleotide phosphate
NADP-MDH	NADP-malate dehydrogenase
NTR	NADPH-dependent Trx reductase
PCR	Polymerase chain reaction
PEG	Polyethylene glycol
Prx	Peroxiredoxin

PSI	Photosystem I
PSII	Photosystem II
ROS	Reactive oxygen species
SDS-PAGE	Sodium lauryl sulfate- polyacrylamide gel
Trx	Thioredoxin

GENERAL INTRODUCTION

Photosynthesis is a process used in plants to transform light energy into chemical energy. However, light as a source of energy is inconstant. To cope with fluctuating light conditions, plants must evolve a number of regulatory system developments. Photosynthesis takes place within the chloroplast. Chloroplasts have to adapt their biochemical pathways to different light conditions for proper metabolism. The light reactions of photosynthesis involve light-driven electron and proton transfers, which occur in the thylakoid membrane. In contrast, the dark reactions involve the fixation of CO_2 into carbohydrates via the Calvin–Benson cycle, which occurs in the stroma [1,2].

Photosynthesis responds to shifting densities of photon flux as light intensities decrease or increase. Light signals received by chlorophyll in chloroplast cause short-term adaptive responses, such as enzyme regulation, photoprotection, and repair [3]. Chloroplasts transmit signals that affect the expression of the protein. One of the primary regulators of photosynthesis-associated nuclear genes is the plastic-to-nucleus signaling. This signaling affects plant cells extensively by enhancing the chloroplast function and coordination [4]. Chloroplasts develop several mechanisms to minimize and deal with reactive oxygen species (ROS), toxic photochemical side reactions [5].

Chloroplasts have a double membrane envelope that consists of an outer membrane and an inner membrane. Thylakoids membranes are packed within both layers (Figure 1). The chlorophyll, a pigment that absorbs the visible spectrum and takes energy from sunlight, is embedded in the thylakoid membrane. The thylakoid membrane system is the place for the light-dependent reactions: it functions as a biological solar cell converting sunlight into an electron transport and a proton gradient across the thylakoid membrane. By contrast,

the chloroplast stroma hosts all light-independent metabolic reactions, including the CO_2 assimilating the Calvin-Benson cycle [6].

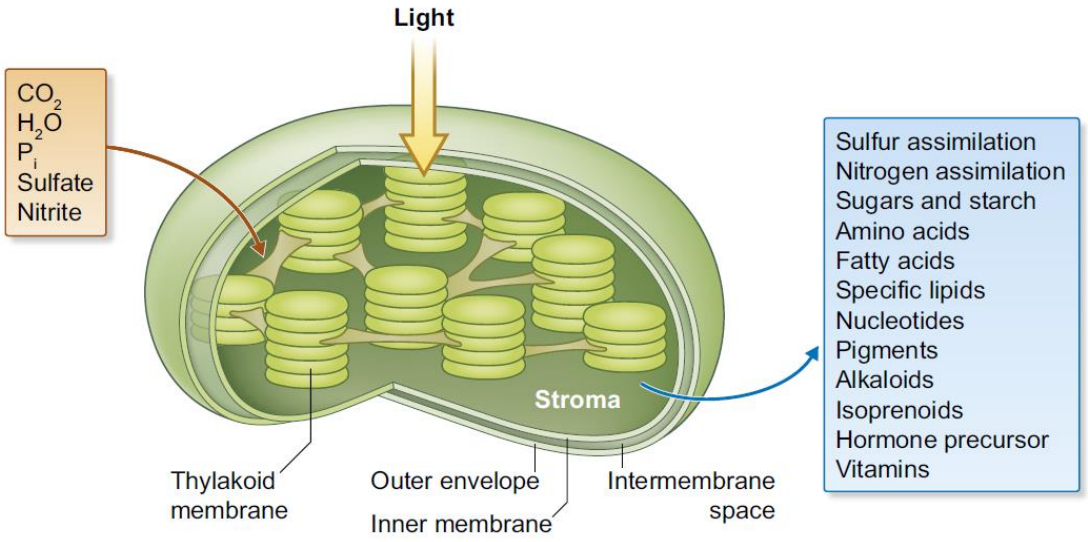

Figure 1 Overall structure of higher plant chloroplasts and overview of its metabolic. The chloroplast collects low energy components (orange box). It transforms them into high-energy metabolites (blue box) by using sunlight energy [6].

Light energy is converted into chemical energy in a protein complex named a photosystem. There are two types of photosystem found in the thylakoid membrane: Photosystem I (PSI) and photosystem II (PSII). PSII is a complex of chlorophyll-protein that uses light to oxidize water to oxygen and reduce the electron acceptor plastoquinone to plastoquinol. Then, plastoquinol carries water-derived electrons to another thylakoid-embedded protein complex, called cytochrome b_6f (cyt b_6f). Cyt b_6f oxidizes plastoquinol to plastoquinone and reduces plastocyanin in the lumen. PSI then carries out a second light-driven reaction. PSI oxidizes plastocyanin and reduces ferredoxin that is a soluble electron

carrier protein. Reduced ferredoxin can then be used by ferredoxin–$NADP^+$ reductase (FNR) to $NADP^+$ to form NADPH. During the electron transport process, the proton is pumped across the thylakoid membrane resulting in an electrochemical proton gradient that drives the ATP synthesis from ADP and inorganic phosphate (Figure 2).

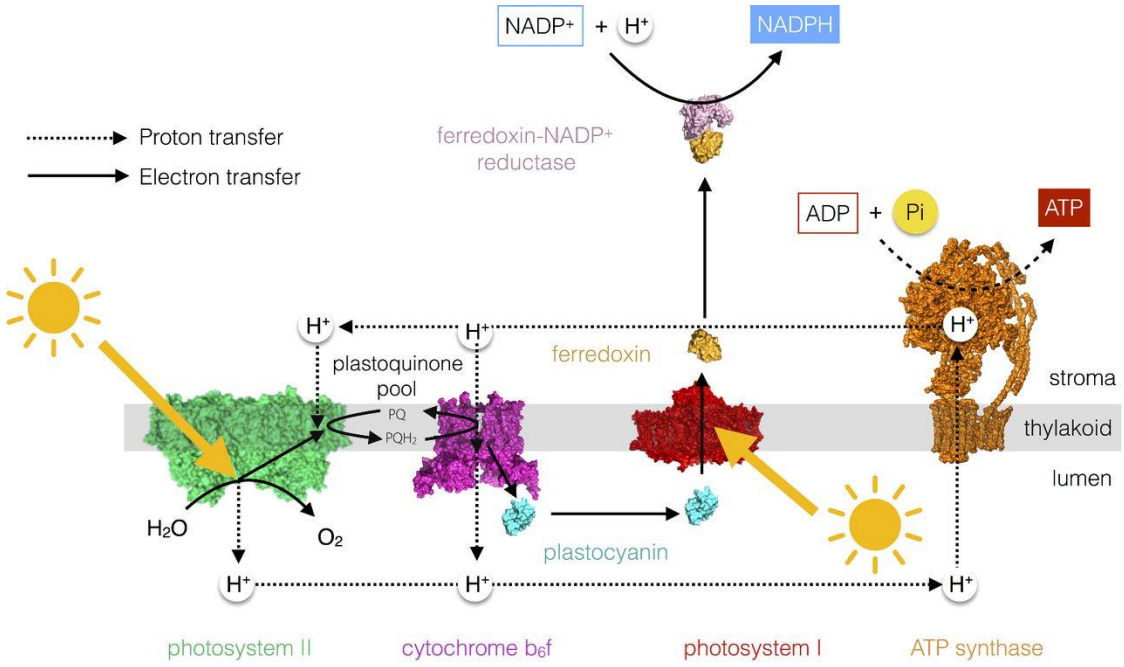

Figure 2 The electron and proton transfer chain in photosynthesis. The linear electron transfer pathway from water to reduce $NADP^+$ to NADPH effects of a proton flux through the ATP synthase enzyme drives ATP synthesis in the stroma [1].

Thiol-based redox regulation is one of the mechanisms to control chloroplast function in response to different light conditions. This regulation controls the activity of target proteins by modifying the Cys residue of the protein, for example, formation or cleavage of a disulfide bond [7–9]. Figure 3 shows this redox regulatory scheme, an electron transported through the photosystem I is sequentially transferred from ferredoxin to

ferredoxin–thioredoxin reductase (FTR), thioredoxin (Trx), and a target enzyme such as fructose 1,6-bisphosphatase (FBPase), sedoheptulose-bisphosphatase, NADP-malate dehydrogenase (NADP-MDH), or 2-Cys peroxiredoxin (Prx) [10–13]. Several redox proteins have an essential role in the redox regulation of the chloroplast and act as information-rich carriers in the signaling cascade for metabolism, antioxidant defense, protein translation, and gene expression [14].

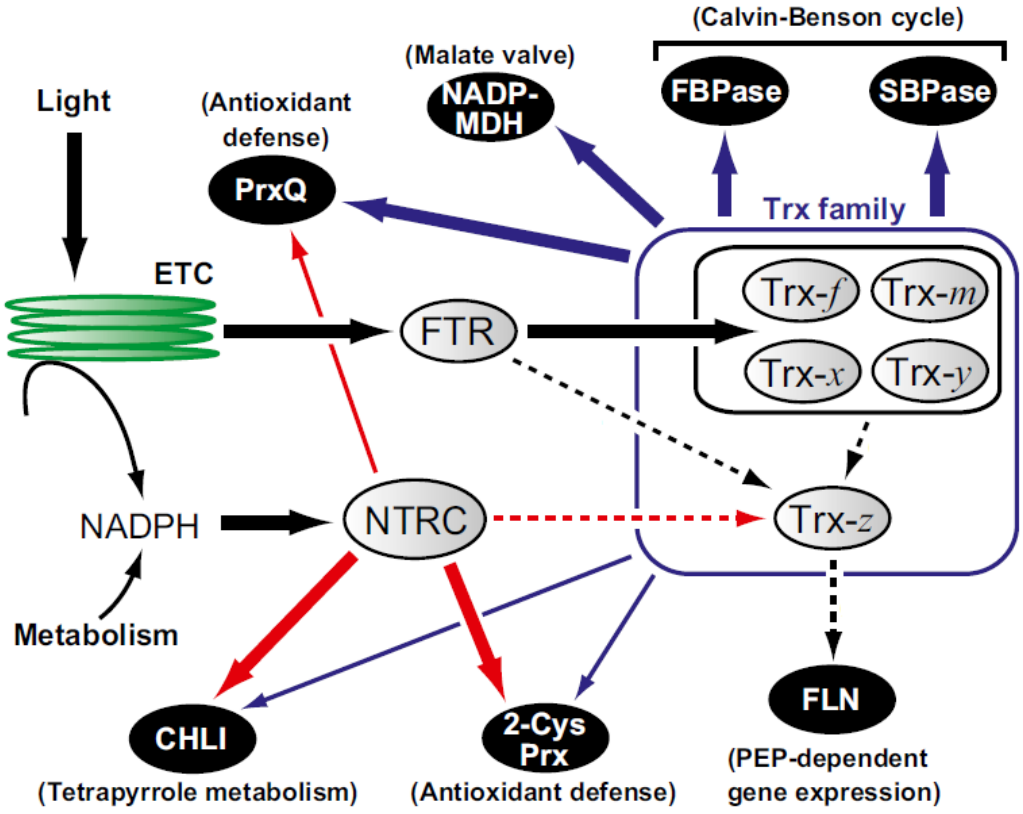

Figure 3 Model of the chloroplast redox network. Distinct target selectivity between NTRC and the Trx family is shown in red and blue arrows, respectively. For common targets, 2-Cys Prx, CHLI, and PrxQ, the difference in reducing power transfer efficiencies is roughly displayed as the thickness of the arrows. Possible redox pathways around Trx-*z* are also shown in dotted arrows. ETC, electron transport chain [15].

FTR is a hetero-dimeric protein that has an iron-sulfur cluster with a redox-active disulfide bridge. It uses the [4Fe-4S] cluster to facilitate the electron transport from the one-electron donor, the [2Fe-2S] cluster of ferredoxins, to the two-electron acceptor, the disulfide bridge of Trxs. The X-ray structure of FTR from *Synechocystis sp.* has been determined at 1.59 Å resolution (PDB ID: 1DJ7) [16]. FTR consists of a catalytic subunit and a variable subunit. The FTR catalytic subunit sequence is highly conserved between species, while the variable subunit sequence is less conserved [17]. The catalytic chain has an α-helical structure containing five helices with a [4Fe-4S] cluster and a redox-active disulfide. The variable chain has an open β-barrel structure containing five antiparallel β-sheet [16].

Trxs are ubiquitous enzymes that control many processes in cell compartments by reducing disulfide bridges in their target proteins. They are able to activate enzymes of the Calvin-Benson cycle and regulate many kinds of chloroplast enzymes involved in other metabolic pathways such as ATP synthase that generates ATP in the light, Acetyl-CoA carboxylase that catalyzes the first step of the fatty acid synthesis, ADP-glucose pyrophosphorylase, glucan:water dikinase and beta-amylase BAM1 involved in starch metabolism, the oxidative pentose phosphate pathway [2,7,18]. Trxs also have the main role in detoxification of ROS and the redox homeostasis maintenance in the chloroplast [7,8,19]. There are ten Trx isoforms in the chloroplast classified into five subtypes (The *f*-, *m*-, *x*-, *y*-, and *z*- types) [20]. The *f*- and *m*- types have the longest history studied in plants. The structures of Trx-*f* and Trx-*m* from spinach have been determined (PDB IDs: 1FAA for Trx-f and 1FB6 for Trx-m). The sequence comparison of the two chloroplast Trxs from spinach shows relatively little resemblance with only 31% identities. However, the structures of

both Trxs are almost similar with r.m.s.d. value of 1.2 Å [21]. Trx structure is characterized by the following succession of secondary structural elements: β1, α1, β2, α2, β3, α3, β4, β5, α4. The Trx fold, as defined by Martin (1995), corresponds to the same succession without α1 and β1 [22].

Dai *et al.* (2007) proposed a Trx reduction mechanism by ferredoxin via FTR based on spectroscopic analysis of the wild type and mutated FTR and structural of ternary ferredoxin:FTR:Trx complex which shown in Figure 4. An electron is transferred from ferredoxin through the Fe-S cluster directly to the disulfide of FTR (C87-C57) in close contact with the cluster in the first reduction step (Rx 1→2). The disulfide bridge cleavage generates a solvent-accessible sulfhydryl (C57) and a solvent-inaccessible C-based thiyl radical (C87). The C87 is stabilized by covalent attachment to the Fe atom of the cluster, forming the sulfur-Fe with five Cys residues. The exposed C57 can act as a nucleophile that attacks and cleaves the disulfide of Trx. This nucleophilic attack results in the formation of intermolecular disulfide between FTR and Trx. After the thiol-disulfide exchange between C57 of FTR and Trx, the disulfide bond of Trx is cleaved, and an FTR:Trx complex with a mixed disulfide bond is formed (species 3). Then a new Fd delivers the second electron either to the one-electron-reduced FTR or to the FTR:Trx complex. Here, the two-electron-reduced species 4 can form, and the reaction pathway splits. In both cases, Fd reduces the iron-sulfur cluster back to its original oxidation state, and C87 is freed. Then C87 attacks the intermolecular disulfide bridge of FTR:Trx complex (short-lived species 5), releasing the fully reduced thioredoxin and the FTR active-site disulfide bond reforms as species 1. The two-electron-reduced FTR species 4, with two free thiols, can instantly reduce and release the reduced Trx [23].

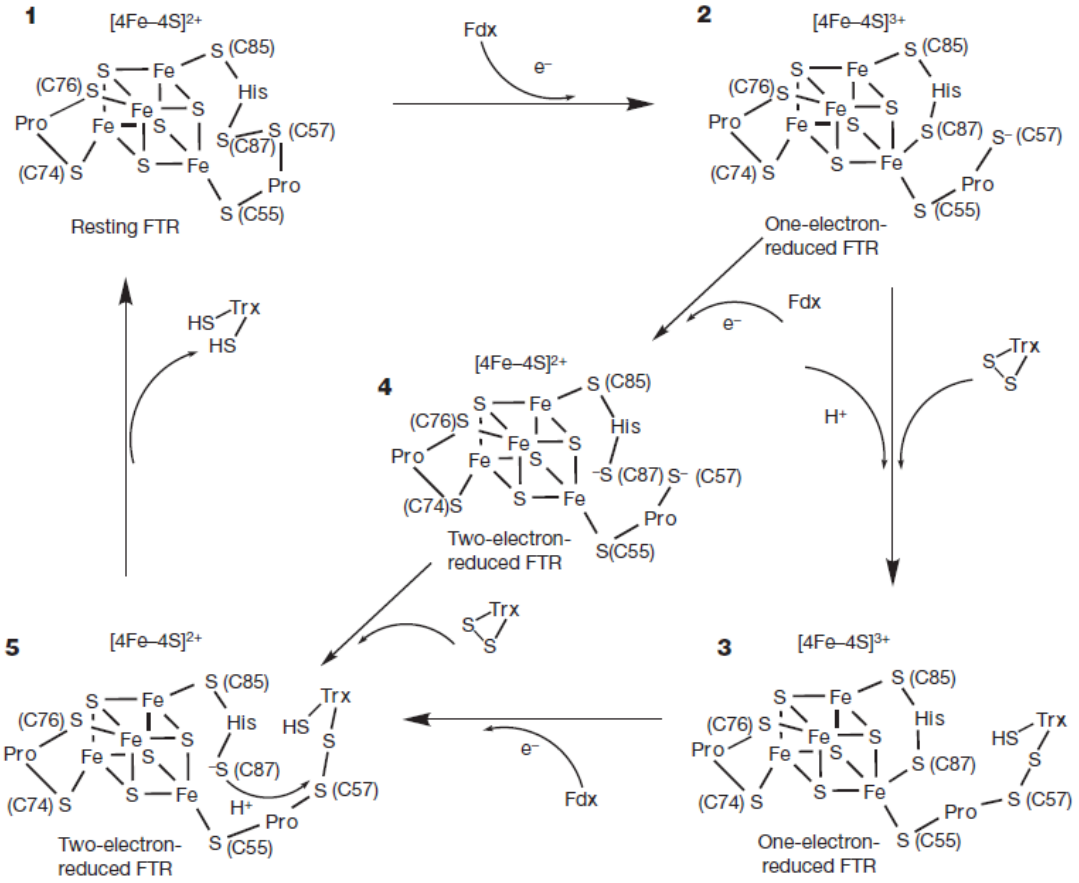

Figure 4 FTR mechanism proposed based on structural and spectroscopic investigations [23].

The completion of the *Arabidopsis thaliana* genome sequence reveals ten chloroplasts Trx isoforms. Compared to multigenic Trx, FTR has less variety of genes. A catalytic subunit of FTR is encoded by a single gene associated with a variable subunit encoded by two genes [24]. Trxs are reduced by FTR or NADPH-dependent Trx reductase (NTR). FTR is the main protein that reduces Trxs in the chloroplast [15].

The redox state determination of ten isoforms from *A. thaliana* shows all chloroplast Trxs can receive electrons from FTR. Based on their kinetic parameters of $S_{0.5}$ and $t_{1/2}$, chloroplast Trxs are classified into three classes, including the high, middle, and low efficiencies, as shown in Figure 5 [25].

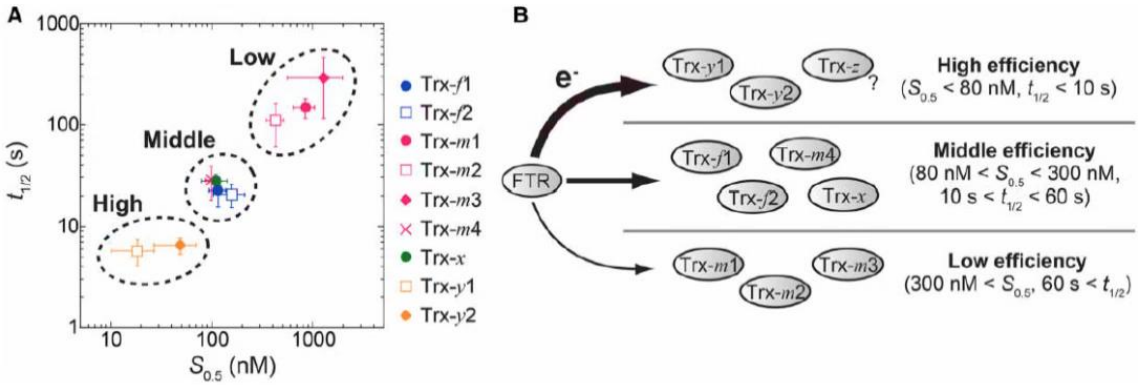

Figure 5 Differential electron transports from FTR to ten chloroplast Trx isoforms in *A. thaliana*. The correlation between two kinetic parameters, $S_{0.5}$ and $t_{1/2}$ (A), and the model of electron transfer from FTR to Trxs (B) are shown [25].

Chloroplast *A. thaliana* has ten Trx isoforms classified into five subtypes (two Trx-*f*, four Trx-*m*, one Trx-*x*, two Trx-*y*, and one Trx-*z*). The determination of the redox potentials of FTR and Trx isoforms raise the question of how FTR (E_m = -356±7 mV) can distinguish between ten homologous Trx isoforms. The E_m value of each Trx has the correlation with the kinetic parameters in part (high: -296 mV < E_m < -296 mV, middle: -321 mV < E_m < -310 mV, low: -335 mV < E_m < -316 mV), but target selectivity of Trxs is not fully controlled by the E_m of Trx. Several structures of Trx from different organisms have been solved by the X-ray crystallography method. Although Trxs proteins have a similar structure named Trx-*f*old, each Trx shows different molecular characteristics,

including target differences and different protein-protein interactions. The crystal structures of the complex between *Synechocystis* FTR and spinach Trx-*f* (PDB ID: 2PU9) or -*m* (PDB ID: 2PUK) have been published. Surprisingly, the interactions of Trx-*f* and -*m* with FTR were found to be highly similar. Nonetheless, the available structures were from two different organisms and therefore difficult to explain the specific interactions of these proteins in vivo.

This research aims to study the structure of FTR:Trx protein complex from each class of activity. I determined the crystal structures of three electron transfer complexes between FTR and Trx from *A. thaliana*; FTR:Trx-*y*1, FTR:Trx-*f*2 and FTR:Trx-*m*2 representing high ($S_{0.5}$ = 18±8 nM, $t_{1/2}$ = 5.7±1.7 s, and E_m = -296 mV), middle ($S_{0.5}$ = 157±54 nM, $t_{1/2}$ = 20.6±5.2 s, and E_m = -321 mV) and low ($S_{0.5}$ = 427±83 nM, $t_{1/2}$ = 110.9±49.9 s, and E_m = -335 mV) FTR:Trx activity class, respectively, to reveal structural differences between the three structures, which offer a plausible explanation for Trx isoform-based fine tuning of FTR activity.

This dissertation consists of Introduction, five Chapters and General discussion; Chapter 1 includes the structure of FTR:Trx-*y*1 complex (high class), Chapter 2, the structure of FTR:Trx-*f*2 complex (middle class), Chapter 3, the structure of FTR:Trx-*m*2 complex (low class), Chapter 4, structure analysis of FTR and Trxs in non-complexed form, and Chapter 5, structural comparison of three FTR:Trx complexes, and General discussion on the FTR affinity differences toward three classes of Trx.

CHAPTER 1

STRUCTURE OF FTR AND TRX-*Y*1 PROTEIN COMPLEX

Introduction

Thioredoxins (Trxs) are small ubiquitous protein with a molecular weight around 12-14 kDa and conserved WC[G/P]PC active site. Plants Trxs are categorized into different types depending on sequence similarity, gene structure, and sub-cellular localization [26,27]. In *Arabidopsis thaliana,* at least 20 Trx isoforms have been reported. There are ten Trx isoforms in the chloroplast divided into five groups (two Trx- *f*, four Trx-*m*, two Trx-*y*, one Trx-*z*, and one Trx-*x*). The WCGPC consensus sequence forms a common active site of chloroplast Trx. Thioredoxin *y*, previously referred to as ch2 in Meyer *et al*. 2002, consists of two members in *A. thaliana*. They cannot activate FBPase and NADP-MDH but can reduce 2-Cys Prx A, B, and Cys Prx Q [20, 27]. Analysis of gene expression reveals that Trx-*y*2 is expressed mostly in leaves and induced by light. In contrast, Trx-*y*1 is expressed in roots, mature siliques, and seeds, indicating that some Trx has many functions besides photosynthesis regulation [28].

Chloroplast Trxs can be reduced by FTR and NTR. FTR is the main protein that reduces Trxs in the chloroplast [29]. Chloroplast FTR is a heterodimer composed of a catalytic subunit 13 kDa associated with a variable subunit of a similar size. In *A. thaliana*, the catalytic subunit is encoded by one gene *FTRC* (At2g04700), and the variable subunit by two genes, *FTRA1* and *FTRA2* (At5g23440 and At5g08410, respectively) [24]. A mutant in one (At5g23440) of the variable subunits was isolated and more sensitive to high light stress [17].

Mutation of the active-site Cys residue of Trx allows stabilizing the transient intermolecular disulfide bridge. This method has been used extensively in FTR-Trx related studies. Using this approach, I generated a covalent bond between wild type FTR and mutant Trx-*y*1. The objective of this study is to analyze the crystal structure of FTR:Trx-*y*1 from *A. thaliana*.

Materials and methods

1. Construction and mutation

Plasmids of wild type FTR and wild type Trx-*y*1 were provided by my collaborator, Hisabori-Wakabayashi Laboratory, Tokyo Institute of Technology Japan. The *FTRA2* and *FTRB* gene fragments encoding the mature protein region of a variable (D73-P184) and catalytic (A32-M146) subunits of FTR, respectively. The *FTRA2* and *FTRB* genes were cloned into the pET-DUET-1 vector (Novagen) (Figure 6 *top*) whereas a gene fragment encoding the mature protein region of Trx-*y*1 was cloned into the pET23a expression vector (Novagen). Mutation C34S was introduced to pET23a-Trx-*y*1 plasmid by Polymerase chain reaction (PCR) mutagenesis using PrimeSTAR MAX DNA Polymerase (Takara Bio Inc. CA, USA) with forward primer 5`-gtggtccttcccagttcatg-3` and reverse primer 5`-catgaactgggaaggaccac-3` (Invitrogen, Thermo Fisher Scientific, Japan) (Figure 6 *bottom*). The sequence of mutation plasmids was confirmed by DNA sequencing using BigDye terminator cycle sequencing kit (Applied Biosystem) and ABI 3130 automated DNA sequencer (Applied Biosystem).

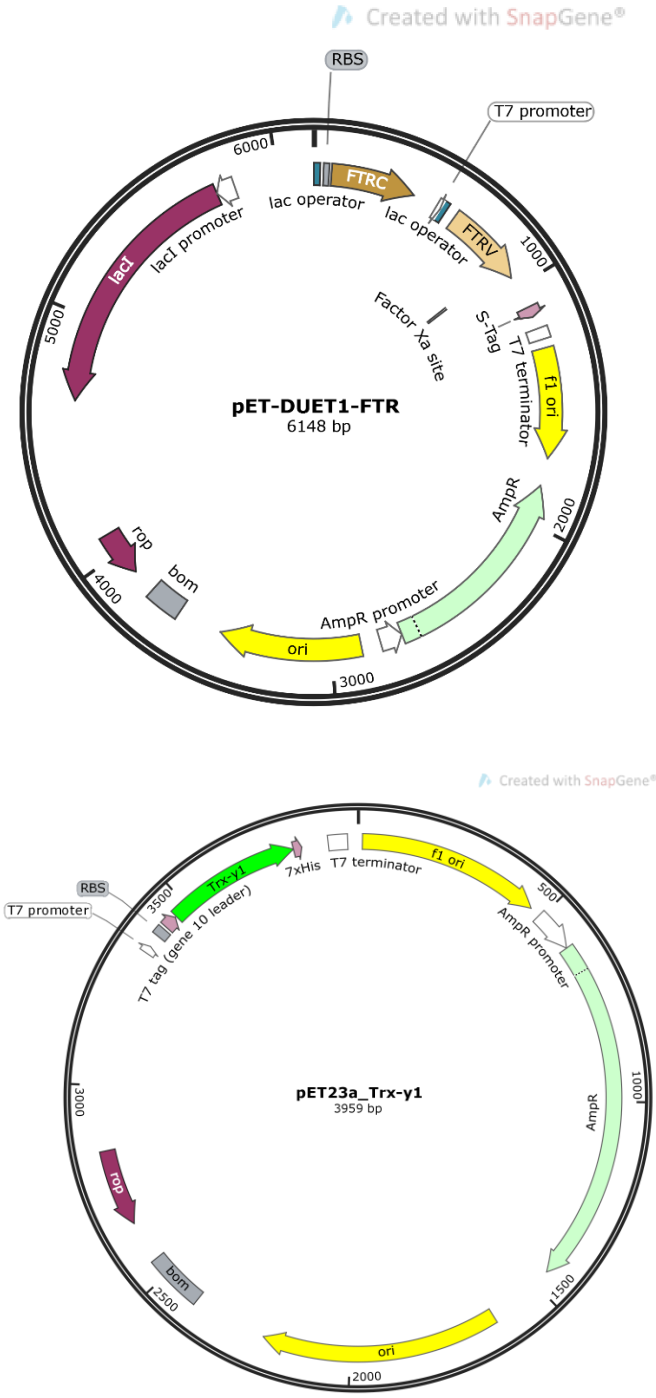

Figure 6 Map of recombinant expression plasmid pET-DUET1-FTR (top) and pET23a-Trx-*y*1 (bottom). Illustrated by SnapGene viewer (from GSL Biotech; available at www.snapgene.com).

2. Protein expression and purification

2.1 Protein expression

Each expression plasmid was transformed into *Escherichia coli* BL21 (DE3). Transformed cells were cultured in Luria-Bertani (LB) broth composed of 1% tryptone, 0.5% yeast extract and 0.5% NaCl at 37 ºC. When the optical density at 600 nm (OD_{600}) reached 0.4 – 0.5, isopropyl-1-thio-β-D-galactopyranoside (IPTG) was added to a final concentration of 0.5 mM to the culture medium and the cells were cultured overnight at 21 ^{0}C. Cells were harvested by centrifugation at 6,000 rpm for 10 minutes using JLA-9.1000 rotor (Beckman Coulter Co., Ltd), and stored at -20°C. The collected cells were used to purify the target protein.

2.2 Protein purification

For purification of FTR heterodimer, the frozen cells were suspended in 25 mM Tris-HCl (pH 7.5) and subsequently disrupted by sonication using BRANSON 450 Sonifire (duty cycle 50% and output control 5 for 3 min). The lysate was clarified by centrifugation at 45,000 rpm for 40 min using HITACHI P45AT rotor, and the supernatant was applied to a DEAE-Toyopearl column (Tosoh). Proteins were eluted with 0-200 mM linear gradient of NaCl in 25 mM Tris-HCl (pH 7.5) by AKTA prime system (GE Healthcare). The fractions containing both subunits were collected, and ammonium sulfate was added to 30% (percent saturation). The protein solution was applied to a Butyl-Toyopearl 650M column (Tosoh). The protein was eluted with 30-0% (percent saturation) inverse gradient of ammonium sulfate in 25 mM Tris-HCl (pH 7.5) by AKTA prime system (GE Healthcare). The protein fraction was collected and applied to a HiPrep 16/60 sephacryl S-100 HR (GE Healthcare). Protein was eluted in 25 mM Trix-HCl (pH 7.5) and 150 mM NaCl by AKTA

purifier system (GE Healthcare). The fractions containing both subunits were collected, diafiltered with 25 mM Tris-HCl (pH 7.5), and finally concentrated using Amicon Ultra-15 Centrifugal Filter Unit (10,000 cutoff molecular mass; Merck Milipore).

For purification of Trx-*y*1, the cells were suspended in 25 mM Tris-HCl (pH 7.5), 1 mM EDTA and 0.5 mM DTT, and subsequently disrupted by sonication using BRANSON 450 Sonifire (duty cycle 50% and output 5 for 3 min). The disrupted cells were centrifuged at 45,000 rpm for 40 min using HITACHI P45AT rotor. The supernatant was applied to a DEAE-Toyopearl column (Tosoh). Proteins were eluted with 0-200 mM linear gradient of NaCl in 25 mM Tris-HCl (pH 7.5), 1 mM EDTA, and 0.5 mM DTT by AKTA prime system (GE Healthcare). The fractions containing Trx were collected, and ammonium sulfate was added to 30% (percent saturation). The protein solution was applied to a Butyl-Toyopearl 650M column (Tosoh). The protein was eluted with 30-0% (percent saturation) inverse gradient of ammonium sulfate in 25 mM Tris-HCl (pH 7.5), 1 mM EDTA, and 0.5 mM DTT by AKTA prime system (GE Healthcare). The fractions containing Trx were collected and applied to a HiPrep 16/60 sephacryl S-100 HR (GE Healthcare). Proteins were eluted in 25 mM Trix-HCl (pH 7.5), 150 mM NaCl, 1 mM EDTA, and 0.5 mM DTT by AKTA purifier system (GE Healthcare). The fractions containing Trx were collected, diafiltered with 25 mM Tris-HCl (pH 7.5), and finally concentrated using Amicon (10,000 cutoff molecular mass; Merck Milipore).

The protein concentration was determined using the molar extinction coefficient (FTR: ε_{415} = 17,400 M^{-1} cm^{-1}, Trx-*y*1: ε_{280} = 11,585 M^{-1} cm^{-1}).

2.3 Complex formation and purification

For initial screening, the concentrated wild type FTR was mixed with an equimolar amount of mutant Trx-*y*1 in the presence of DTT. For optimization of crystallization, the concentrated wild type FTR was combined with an excess amount of mutant Trx-*y*1 in the presence of DTT. The mixture was incubated for 10 min at 4 ºC and dialyzed overnight with 25 mM Tris-HCl (pH 7.5) using dialysis cassette G2 (0.5 mL capacity and 10,000 cutoff molecular mass, Thermo Scientific, USA). The FTR:Trx-*y*1 complex was applied to HiTrap SP HP 5 mL column (GE Healthcare). The column was washed with 25 mM Tris-HCl (pH 7.5). After the flow-through was out, an anion Q HP 5 mL column (GE Healthcare) was attached below the SP HP column. The proteins were eluted with 0-500 mM linear gradient of NaCl in 25 mM Tris-HCl (pH 7.5) by AKTA purifier system (GE Healthcare). The fractions containing FTR:Trx-*y*1 complex were collected, concentrated and diafiltered with 25 mM Tris-HCl (pH 7.5).

3. Crystallization and structure determination

The initial screening of FTR:Trx-*y*1 complex was performed by sitting-drop vapor diffusion method using ten commercial screening kits, Crystal screen I and II, Peg Rx I and II, Peg ion 1 and 2 (Hampton Research, Aliso Viejo, CA, USA), and Wizard I, II, III, and IV (Rigaku, Bainbridge Island, WA, USA), at 4 ºC and 20 ^{0}C. The sample concentration for crystallization was 10 mg mL^{-1} of FTR in 25 mM Tris-HCl (pH 7.5). I used the crystallization robot, Mosquito LCP (TTP Labtech) for screening. The droplets containing 0.2 µL protein complex with 0.2 µL reservoir solution were equilibrated with 80 µL reservoir at 4 ºC and 20 ºC. After crystals were obtained in the initial screen, the

crystallization conditions were optimized by the hanging-drop vapor diffusion method using different precipitating agents and additives around the initial conditions. The mixture of 1 µL sample complex and 1 µL reservoir buffer was put on the cover slide, flip it gently, and lay in down on top of the well containing 150 µL crystallization buffer. The plate which contains 48 wells was incubated at 20 °C and checked from time to time.

The crystals of FTR:Trx-*y*1 (10 mg mL^{-1}) were obtained in 100 mM magnesium citric acid (pH 3.5), 5% (v/v) 2-propanol, and 5-9% (w/v) PEG 3,350 at 20 ^{0}C. After the crystals were grown enough to be checked, the crystal was picked using a loop, briefly soak into the cryoprotectant solution comprised crystallization buffer with an additional 30% (v/v) glycerol, and quickly frozen in liquid nitrogen. The crystals were kept in the liquid nitrogen until they are used for the X-ray diffraction experiment.

The X-ray diffraction data of FTR:Trx-*y*1 were collected a wavelength of 0.9000 Å on beamline BL44XU at SPring-8 synchrotron radiation (Hyogo, Japan) using EIGER X16M (Dectris, Baden, Switzerland). The diffraction data were collected at 100 K and processed using XDS [30]. The protein complex structure was determined by molecular replacement with program PHASER in the CCP4 program package [31] using *Synechocystis* FTR and mutant spinach Trx-*f* (PDB ID 2PU9) as a search model. The structure of FTR:Trx-*y*1 complex was refined with PHENIX [32]. Figures were prepared using PyMol (The PyMOL Molecular Graphic System, Version 2.0 Schrödinger, LLC), and protein-protein interactions were checked by Dimplot in Ligplot+ [33].

Results

Protein expression and purification

Each recombinant plasmid of FTR and Trx-*y*1 was used in the transformation of *E. coli* BL21 (DE3). The cells were cultured in LB medium until OD_{600} reached 0.5-0.8 then induced with a final concentration 0.5 mM IPTG at 21 °C overnight. Cultured cells were collected and disrupted by sonication. Both FTR and Trx-*y*1 protein were purified using the same purification steps: (1) anion exchange chromatography using anion exchange DEAE-Toyopearl column, (2) hydrophobic chromatography using hydrophobic butyl-Toyopearl column, and (3) size exclusion chromatography using sephacryl S-100 column. The protein was checked by 15% SDS-PAGE (Figure 7). The protein concentration was calculated using the molar extinction coefficient (FTR: ε_{415} = 17,400 M^{-1} cm^{-1}, Trx-*y*1: ε_{280} = 11,585 M^{-1} cm^{-1}). The yield of FTR protein was 6.4 mg per 1-liter culture. Trx-*y*1 protein was overexpressed with a yield of around 39 mg per 1-liter culture.

The concentrated wild type FTR was mixed with an excess amount of mutant Trx-*y*1 in the presence of DTT. The mixture was incubated for 10 min at 4 °C and dialyzed overnight with 25 mM Tris-HCl (pH 7.5). The FTR:Trx-*y*1 complex was repurified by cation SP and anion Q columns to remove the contaminant and unreacted protein from the complex. The protein was washed with 25 mM Tris-HCl (pH 7.5). After the flow-through that contained the excess Trx-*y*1 protein was out, an anion column was attached below the cation column. The protein was then eluted with 0-500 mM linear gradient of NaCl in 25 mM Tris-HCl (pH 7.5). The fractions that consisted of FTR and Trx proteins were concentrated and diafiltered in 25 mM Tris-HCl (pH 7.5) for crystallization (Figure 8).

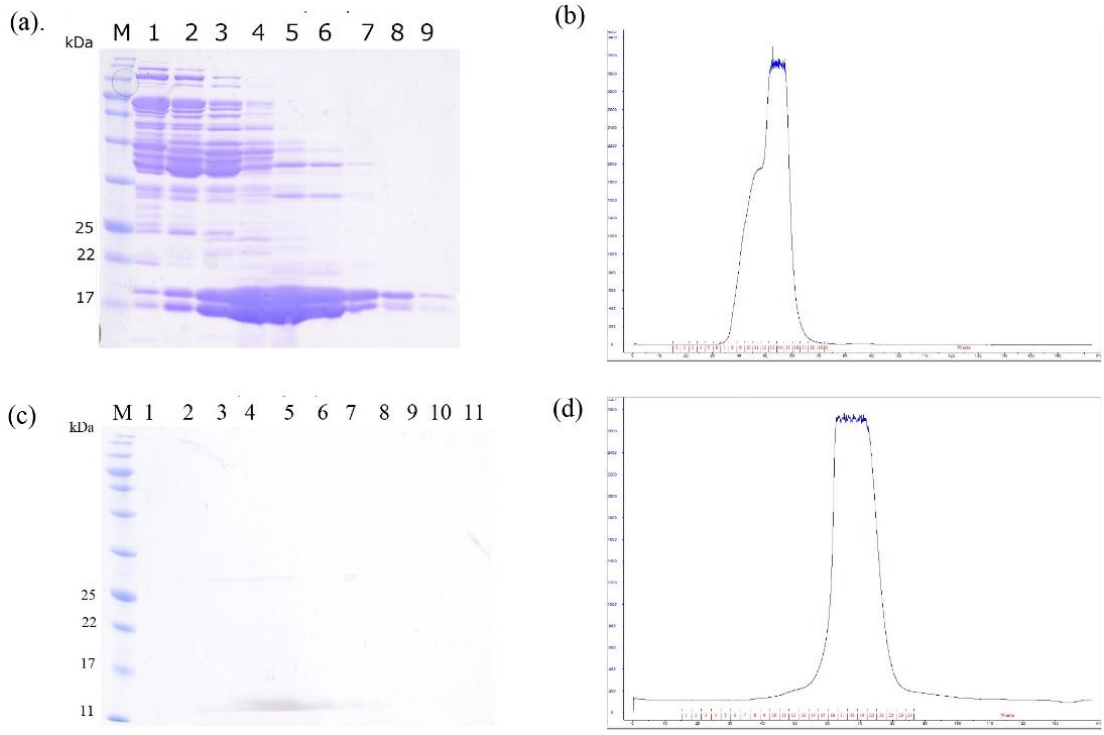

Figure 7 SDS-PAGE and chromatogram of FTR and Trx-*y*1 at the final purification step. (a) SDS-PAGE and (b) chromatogram of FTR at the gel filtration step. Lane M, protein marker; lane 1-9, elution 8^{th}-16^{th} fractions. 10^{th}-13^{th} fractions were collected. (c) SDS-PAGE and (d) chromatogram of Trx-*y*1 at the gel filtration step. Lane M, protein marker; lane 1-11, elution 14^{th}-24^{th} fractions. 14^{th}-24^{th} fractions were collected.

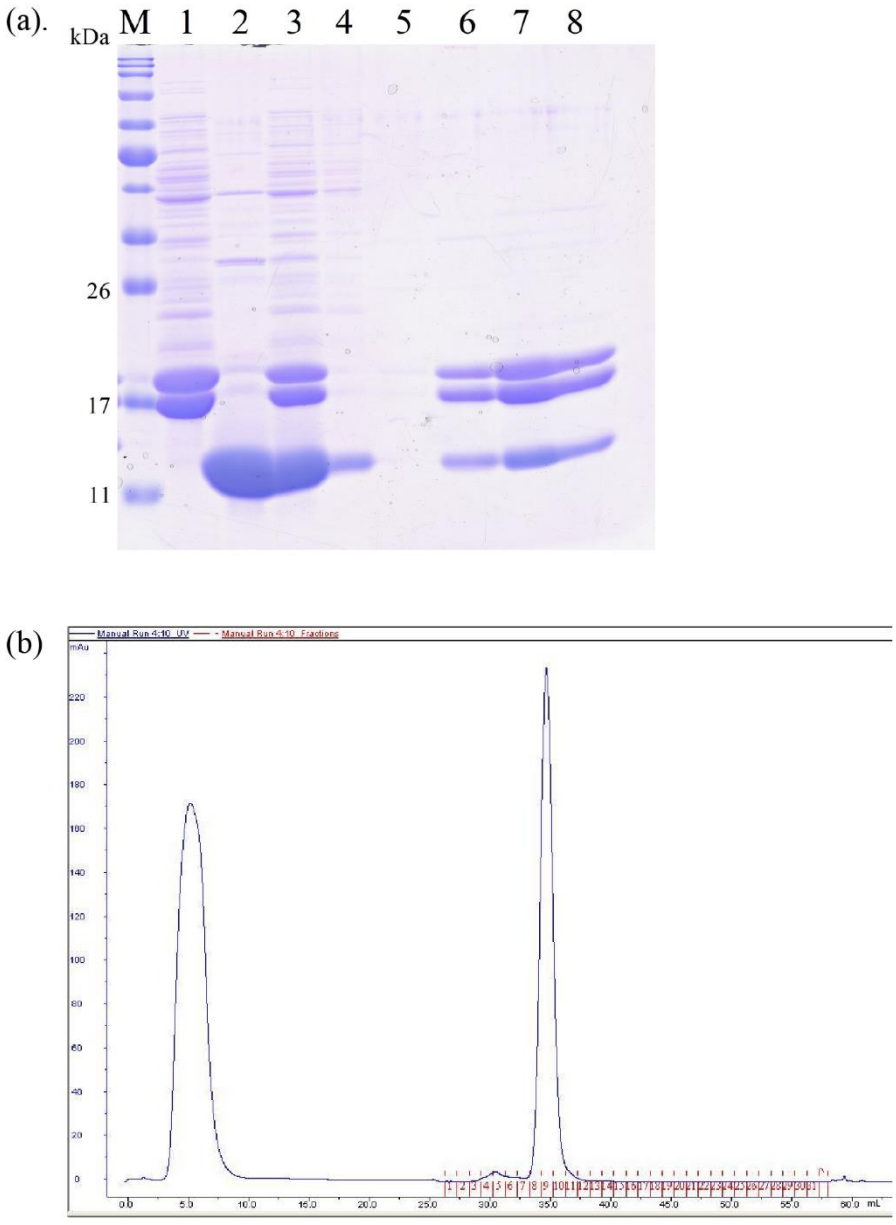

Figure 8 SDS-PAGE and chromatogram of FTR:Trx-*y*1 complex after cation SP and anion Q columns; Lane M, protein marker; lane 1, purified FTR protein; lane 3, purified Trx-*y*1 protein; lane 4, the mixture of FTR and Trx-*y*1; lane 4, flow-through; lane 5-8, elution 8^{th}-11^{th} fractions. 9^{th}-11^{th} fractions were collected for crystallization.

Crystallization, data collection and structure determination

The FTR:Trx-*y*1 complex with a concentration of FTR around 10 mg mL^{-1} was used for crystallization. The sample buffer consists of 25 mM Tris-HCl (pH 7.5). The initial screening was performed using commercial screening kits with the sitting-drop vapor diffusion method. The droplets, the mixture of 0.2 µL protein complex with 0.2 µL reservoir solution, were equilibrated with 80 µL reservoir at 4 ºC and 20 ºC. Needle and Sea urchin-like crystals were grown in several conditions. The crystallization conditions were further optimized by the hanging-drop vapor diffusion method using different precipitating agents and additives around the initial conditions. The droplets containing 1 µL complex and 1 µL reservoir buffer were equilibrated in 150 µL reservoir buffer. The needle-like crystals of FTR:Trx-*y*1 were obtained in 100 mM magnesium citric acid (pH 3.5), 5% 2-propanol, and 5-9% PEG 3,350 at 20 ^{0}C, as shown in Figure 9. The crystals were soaked into the cryoprotectant solution containing the crystallization buffer with additional 30% glycerol and quickly frozen in liquid nitrogen.

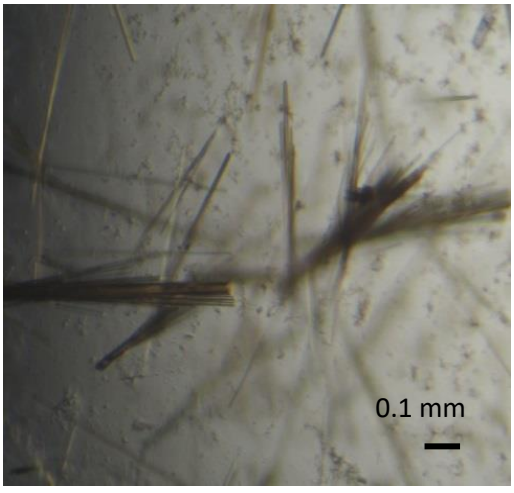

Figure 9 Crystals of FTR:Trx-*y*1 complex.

The X-ray diffraction images were collected at a wavelength of 0.9000 Å on beamline BL44XU at SPring-8 synchrotron radiation (Hyogo, Japan) using EIGER X16M (Dectris, Baden, Switzerland). The crystal of FTR:Trx-*y*1 complex belonged to the orthorhombic group $P2_12_12_1$ with unit cell parameter a = 54.96, b = 60.76, c = 61.06 Å. The Matthews coefficient was 2.00 with one molecule in the asymmetry unit and 38.58% solvent content [34]. The molecular replacement was performed using program PHASER in the CCP4 program suite [35] with *Synechocystis* FTR and spinach Trx-*f* (PDB ID 2PU9) as a search model. The structure model was built manually using COOT [36], and structural refinement was performed using PHENIX.refine program in PHENIX [37]. The values of *R*-work and *R-f*ree were 16.99% and 19.29%, respectively. The final crystallographic data and refinement statistics are listed in Table 1.

Table 1 Data collection and refinement statistics.

Data collection	
Wavelength (Å)	0.9000
Resolution range (Å)	43.07-1.59 (1.69-1.59)
Space group	$P2_12_12_1$
Unit cell	
a, b, c (Å)	54.96, 60.76, 61.06
α, β, γ (º)	90, 90, 90
Total reflections	184414 (27906)
Unique reflections	27938 (4419)
Multiplicity	6.6 (6.3)
Completeness (%)	99.8 (99.1)
Mean I/sigma(I)	10.40 (3.03)
*R-m*erge	0.12 (0.736)
*R-m*eas	0.13 (0.754)
$CC_{1/2}$	0.995 (0.903)
Refinement	
Reflections used in refinement	27910
Reflections used for *R-f*ree	1397
R-work (%)	16.99
*R-f*ree (%)	19.29
Number of non-hydrogen atoms	1841
macromolecules	1725
ligands	8
solvent	108
RMS (bonds) (Å)	0.018
RMS (angles) (º)	1.41
Ramachandran favored (%)	98.10
Ramachandran allowed (%)	1.90
Ramachandran outliers (%)	0.00
Clashscore	2.63
Average B-*f*actor ($Å^2$)	22.42
macromolecules	22.00
ligands	12.70
solvent	29.77
PDB ID	

Statistics for the highest-resolution shell are shown in parentheses.

Discussion

This chapter discuss the crystal structure of complex protein between FTR and Trx-*y*1 from *A. thaliana*. The structure was solved at 1.59 Å resolution and composed of one catalytic subunit of FTR and one Trx-*y*1 (Figure 10a). The electron density was clear enough to refine the model without any ambiguity of chain assingment. The recombinant catalytic subunit of FTR protein has 115 amino acid residues, and the Trx-*y*1 protein has 110 amino acid residues. The structure model of FTRC protein missed the first three amino acid residues at N-terminal whereas the model of Trx-*y*1 protein missed the first five amino acid residues at N-terminal and the last three amino acid residues at C-terminal.

The catalytic subunit of FTR from *A. thaliana* had a similar structure with *Synechocystis* FTR (PDB ID 1DJ7). It is comprised of five α-helices with loops between the helices consisting of the iron-sulfur cluster and active site cysteine residues. Trx-*y*1 had four-stranded mixed β-sheets, flanked by four helices which form thioredoxin fold. There was an intermolecular disulfide bridge between C56 of FTRC and C31 of Trx-*y*1 (Figure 10a). Unexpectedly, the variable subunit of FTR was missing and replaced by another Trx-*y*1, a crystallographic symmetry mate (Figure 10b). It was confirmed by SDS-PAGE (Figure 11). The sample protein for crystallization was contained Trx-*y*1, catalytic and variable subunit of FTR whereas the crystal of FTR:Trx-*y*1 consisted of Trx-*y*1 and only a catalytic FTR subunit. During crystallization, the variable subunit of FTR was thus lost. The chemical composition of the crystallization buffer possibly weakened the intramolecular interactions between FTR subunits. It may reinforce the non-physiological intermolecular interactions between the catalytic subunit and the next molecule of Trx-*y*1.

The high concentration of protein samples in the crystallization droplet may also accelerate this non-physiological swapping of interacting partners.

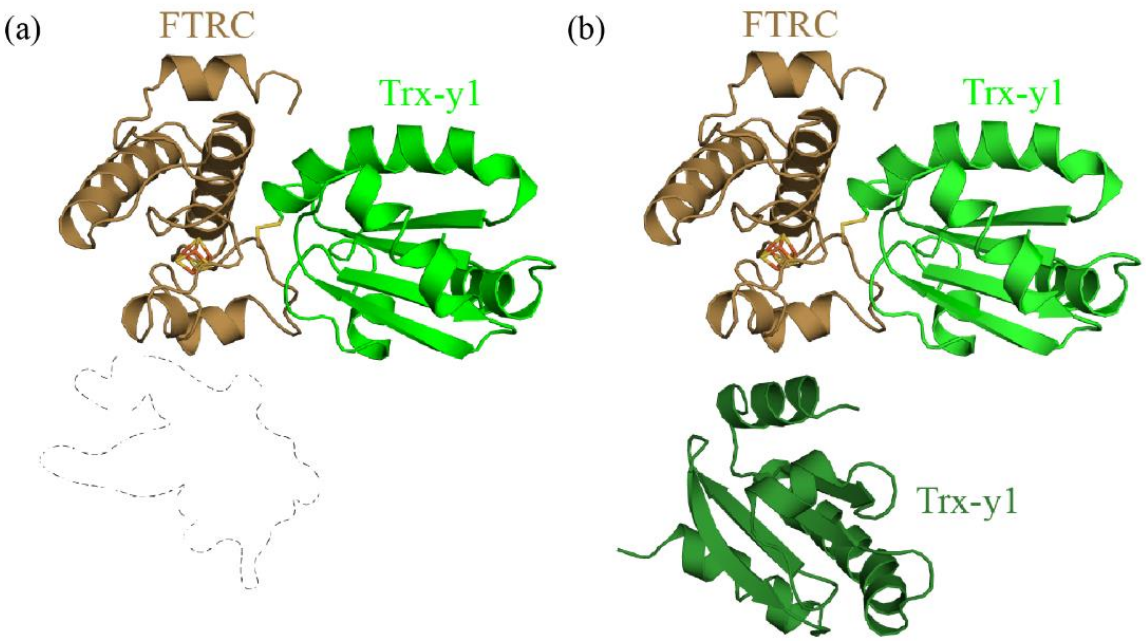

Figure 10 Overall structure of the FTR:Trx-*y*1 complex. The catalytic subunits of FTR, Trx-*y*1, and crystallographic-symmetry-related Trx-*y*1 are shown in brown, green, and dark green, respectively. The FTR variable subunit was missing. The iron-sulfur cluster and disulfide bridge are shown in yellow-orange and yellow sticks, respectively.

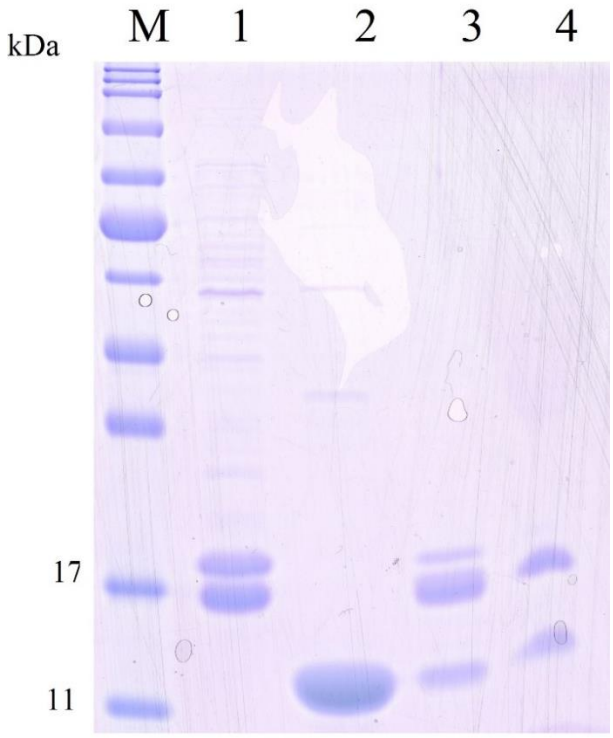

Figure 11 SDS-PAGE of monomer FTR and Trx-*y*1, and FTR:Trx-*y*1 complex. Lane 1, FTR protein; lane 2, Trx-*y*1 protein; lane 3, crystallization sample of FTR:Trx-*y*1 complex; lane 4, the crystal of FTR:Trx-*y*1.

In the crystal structure, the interaction of FTRC with Trx-*y*1 occurred through two distinct interfaces. FTRC interacted with Trx-*y*1 in the same unit cell (green) at the first interface and with another Trx-*y*1', a crystallographic symmetry mate of Trx-*y*1 (dark green) at the second interface (Figure 10). The first interface interaction was displayed in Figure 12 and Figure 13a. The residue R57 of FTRC formed salt bridge with E72 of Trx-*y*1. The side chain of K62 of FTRC interacted with the side chain of E60 of Trx-*y*1 through hydrogen bonds. The main chain carbonyl oxygen of C56 and H58 of FTRC formed hydrogen bonds with the amide of nitrogen of L74 and E72 of Trx-*y*1. The FTR:Trx-*y*1

complex was also stabilized via hydrophobic interaction which formed by the residues D31, V34, V37, V38, K40, G41, P55, C56, R57, H58, K62, H85, C86, M87, F96, M115 of FTR and the residues T29, W30, C31, G32, P33, Q35, F36, E60, A66, I71, E72, A73, L74, A92 of Trx-*y*1 (Figure 13a).

In the *Synechocystis* FTR structure, the essential interactions between FTR subunits are hydrogen bonds between side chains E81 and R82 (E80 and R81 in *A. thaliana* numbering) of the catalytic subunit and side chain H64 and E69 of the variable subunit, respectively [38]. The interactions of FTR:Trx-*y*1' complex crystals at the second interface were shown in Figure 13b. The residues E80 and R81 of FTRC interacted with D13 of Trx-*y*1' via hydrophobic interaction and hydrogen bonds interaction. Moreover, the residue D13 is unique to Trx-*y*1'. This residue was substituted by I21 and S20 in Trx-*f*2 and Trx-*m*2 sequences, respectively. The residue Q68 of FTRC formed hydrogen bonds to residue N17 of Trx-*y*1' via water. Besides this, several hydrophobic interactions were formed by residues F70, V76, P77, E80, R81 of FTRC and D9, D13, V16, N17 of Trx-*y*1'. The crystallization condition may disrupt the important interactions of FTR subunits; simultaneously, the high concentration of protein may exaggerate the interaction between the catalytic subunit of FTRC and Trx-*y*1' at the second interface.

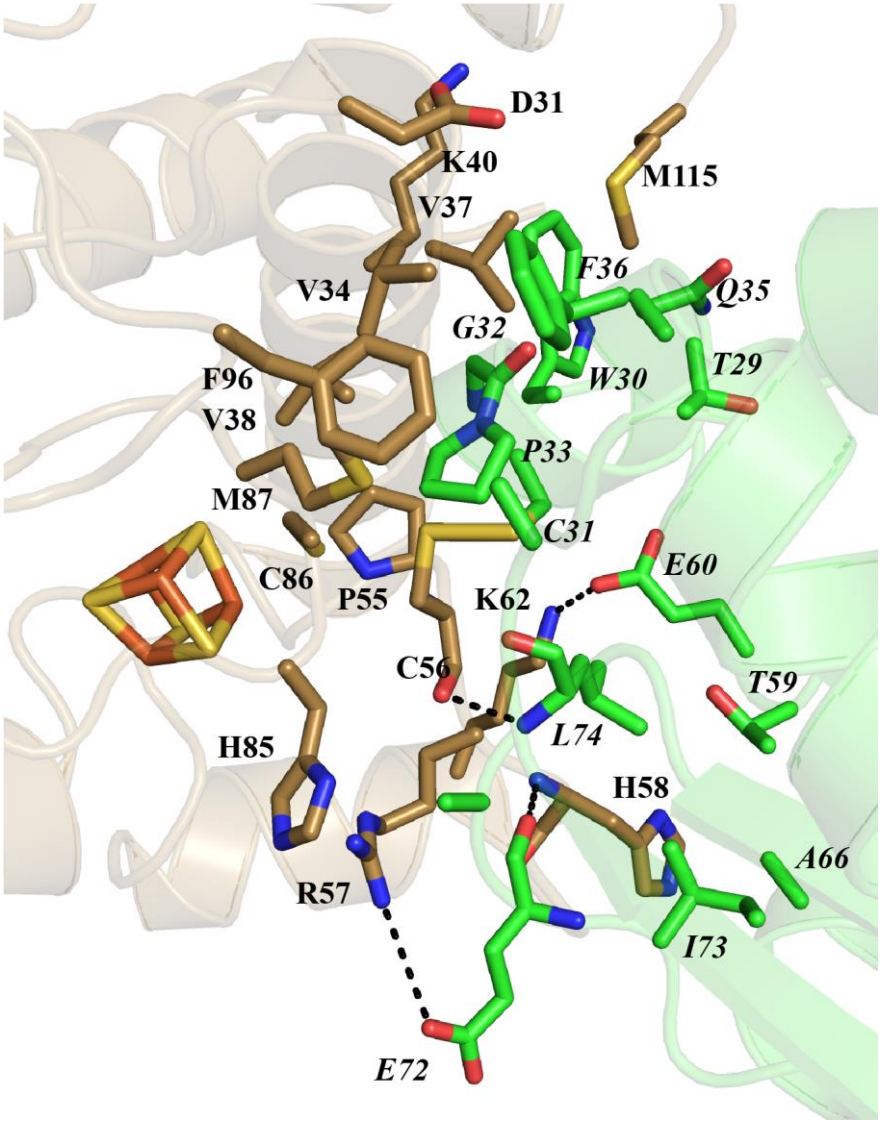

Figure 12 The interactions between the catalytic subunit of FTR (brown) and Trx-*y*1 (green). An intermolecular disulfide bridge between C56 of FTR and C31 of Trx-*y*1, resembling the intermediate in the reaction, links the active sites of FTR and the Trx. Hydrogen bonds are represented as black dash. Labels for amino acids in FTR and Trx are shown in bold and bold italics, respectively.

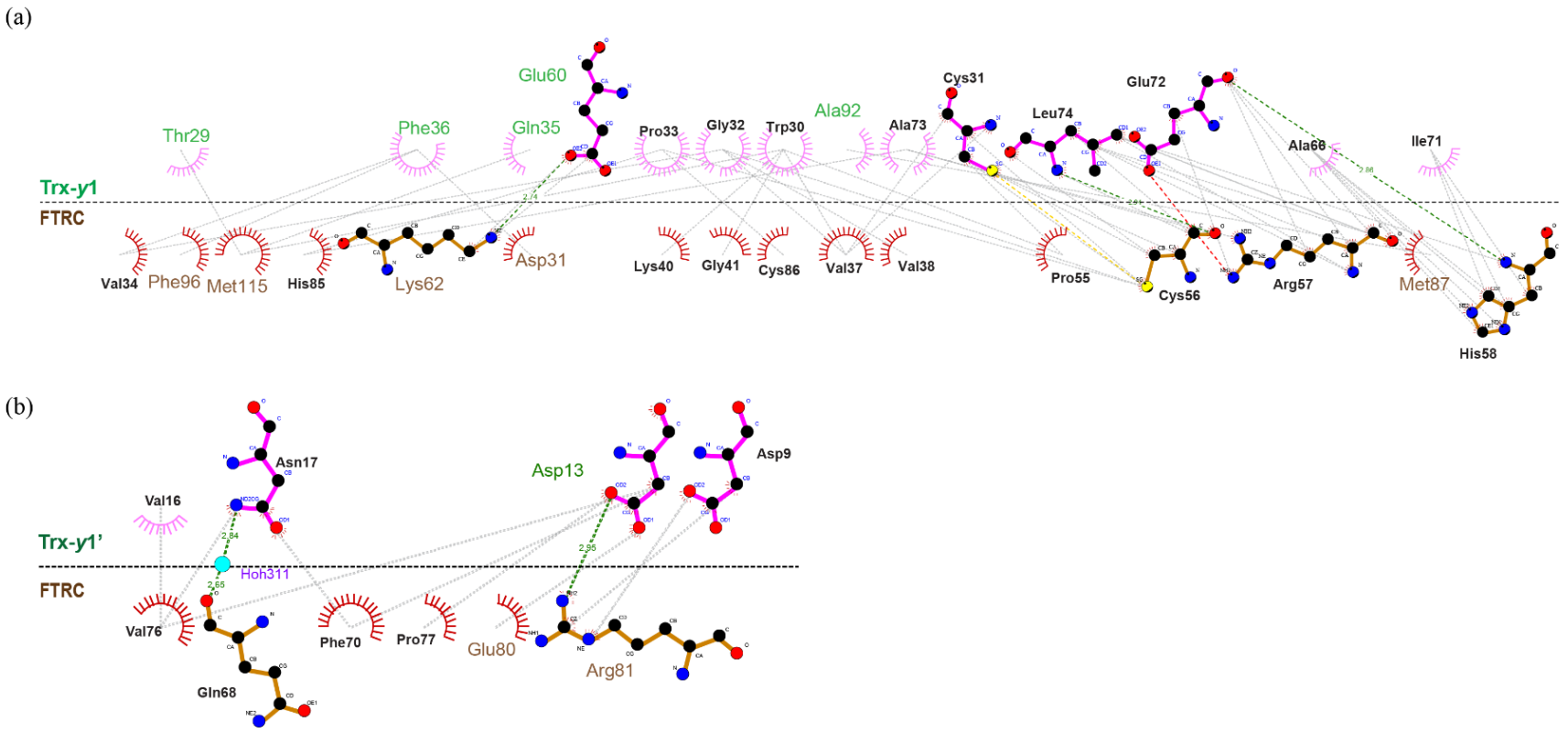

Figure 13 Interaction between catalytic subunit of FTR with (a) Trx-*y*1 and (b) crystallographic-symmetry-related Trx-*y*1. Illustrated by Dimplot in Ligplot+ [33]. Hydrogen bond interaction is shown in green dash and hydrophobic interaction is shown in red dash.

CHAPTER 2

STRUCTURE OF FTR AND TRX-*F*2 PROTEIN COMPLEX

Introduction

Thioredoxins are small ubiquitous protein (around 12 kDa). Trx has a conserved WCGPC motif at an active site to process a dithiol-disulfide exchange reaction with the target enzymes. The completion of the genome of *A. thaliana* revealed at least 46 Trx family, including Trx isoform and Trx-like proteins. In the chloroplast, Trxs are encoded by ten genes and classified into five types: two Trx-*y*, four Trx-*m*, two Trx-*f*, one Trx-*x*, and one Trx-*z* [20,39]. One of them is Trx-*f* that has been studied well for more than 40 years. Trx-*f* has two members which are Trx-*f*1 and Trx-*f*2. They can reduce target proteins such as FBPase, MDH, 2-Cys Prx A, and B as well as Cys Prx Q [20].

To date, the structure of *Synechocystis* FTR and mutant spinach Trx-*f* has been determined (PDB ID 2PU9). It revealed that Trx-*f* interacted only with the catalytic subunit of FTR. This chapter aims to study the complex structure between FTR and Trx-*f*2 from the same species, *A. thaliana*.

Materials and methods

1. Construction and mutation

The gene fragment encoding the mature protein region (D71-G185 of At5g16400) of Trx-*f*2 was clone into the pET-23a expression vector. The recombinant C42S mutant of pET23a-Trx-*f*2 plasmid was engineered (Figure 14) by PCR mutagenesis using

PrimeSTAR MAX DNA Polymerase (Takara Bio Inc. CA, USA) with forward primer 5`-gtgtggtccttccaaagtg-3` and reverse primer 5`-cactttggaaggaccacac-3` (Invitrogen, Thermo Fisher Scientific, Japan). The sequence of mutation plasmids was confirmed by DNA sequencing using BigDye terminator cycle sequencing kit (Applied Biosystem) and ABI 3130 automated DNA sequencer (Applied Biosystem). The recombinant proteins of FTR and Trx:*f*2 from *A. thaliana* were expressed and purified, as previously described in Chapter 1.

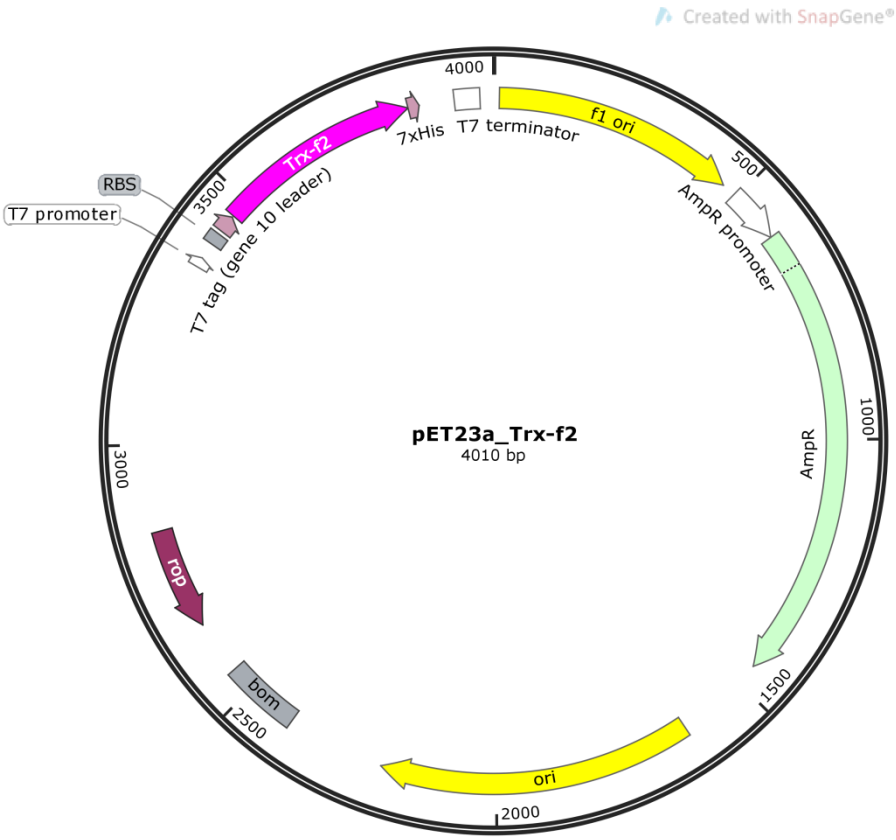

Figure 14 Map of recombinant expression plasmid pET23a-Trx-*f*2. Illustrated by SnapGene viewer (from GSL Biotech; available at www.snapgene.com).

2. Crystallization and structure determination

Complex formation of FTR:Trx and its purification were similarly performed as described in Chapter 1. Crystallization trials of FTR:Trx-*f*2 complexes were conducted by the sitting-drop vapor diffusion method at 20 ^{0}C. I used the crystallization robot, Mosquito LCP (TTP Labtech), for initial screening. The commercial screening kits which were used in the initial trials were Crystal screen I and II, Peg ion 1 and 2, Peg Rx I and II (Hampton Research, Aliso Viejo, CA, USA), and Wizard I, II, III, and IV (Rigaku, Bainbridge Island, WA, USA). The sample concentration for crystallization was 10 mg mL^{-1} of FTR in 25 mM Tris-HCl (pH 7.5). After crystals were obtained in the initial screen, the crystallization conditions were optimized by the hanging-drop vapor diffusion method using varying the precipitant concentration around the original conditions.

The crystals of FTR:Trx-*f*2 (10 mg mL^{-1}) were obtained in 200 mM magnesium nitrate and 16-20% PEG 3,350 at 20 ^{0}C. After the crystals were grown enough to be checked, the crystal was picked using a loop, briefly soak into the cryoprotectant solution composing crystallization buffer with additional 25% glycerol, and quickly frozen in liquid nitrogen. The crystals were kept in the liquid nitrogen until they are used for X-ray diffraction experiment.

X-ray diffraction data of FTR:Trx-*f*2 were collected using an X-ray of a wavelength of 0.9000 Å on beamline BL44XU at SPring-8 synchrotron radiation facility (Hyogo, Japan) using EIGER X16M detector (Dectris, Baden, Switzerland). The diffraction data were collected at 100 K and processed using XDS [30]. The protein complex structure was determined by molecular replacement with program PHASER in the CCP4 program package [31] using *Synechocystis* FTR and mutant spinach Trx-*f* (PDB ID 2PU9) as a

search model. The structure of FTR:Trx-*f*2 complex was manually built with COOT [36] and refined with PHENIX [32]. Figures were prepared using PyMol (The PyMOL Molecular Graphic System, Version 2.0 Schrödinger, LLC), and protein-protein interactions were checked by Dimplot in Ligplot+ [33].

Results

Protein expression and purification

E. coli BL21 (DE3) was transformed with each recombinant plasmid pET-DUET1-FTR and pET23a-Trx-*f*2. The transformant cells were grown on LB medium until OD_{600} 0.5-0.8 and followed by induction with a final concentration of 0.5 mM IPTG at 21 ºC overnight. The cells were disrupted by sonification, and the lysates were clarified by centrifugation. The purification of FTR was previously described in Chapter 1. For Trx-*f*2 purification, the crude sample was applied to the anion exchange chromatography column. The protein was out in the flow-through during washing with 25 mM Tris-HCl (pH 7.5) and further purified by hydrophobic and size exclusion chromatography. The purified protein was checked by SDS-PAGE (Figure 15). The yield of Trx-*f*2 was relatively high, approximately 22.44 mg per 1-liter culture.

The complex of FTR:Trx-*f*2 was obtained by mixing wild type FTR with an excess amount of Trx-*f*2 in the presence of DTT. The mixture was dialyzed overnight with 25 mM Tris-HCl (pH 7.5) and repurified on the next day using a combination of cation and anion columns (Figure 16). The contamination protein was in the flow-through while the unreacted Trx-*f*2 was eluted before the elution of complex. Fractions 5^{th} to 8^{th} containing

FTRC, FTRV, and Trx-*f*2 were collected and concentrated in 25 mM Tris-HCl (pH 7.5) for crystallization.

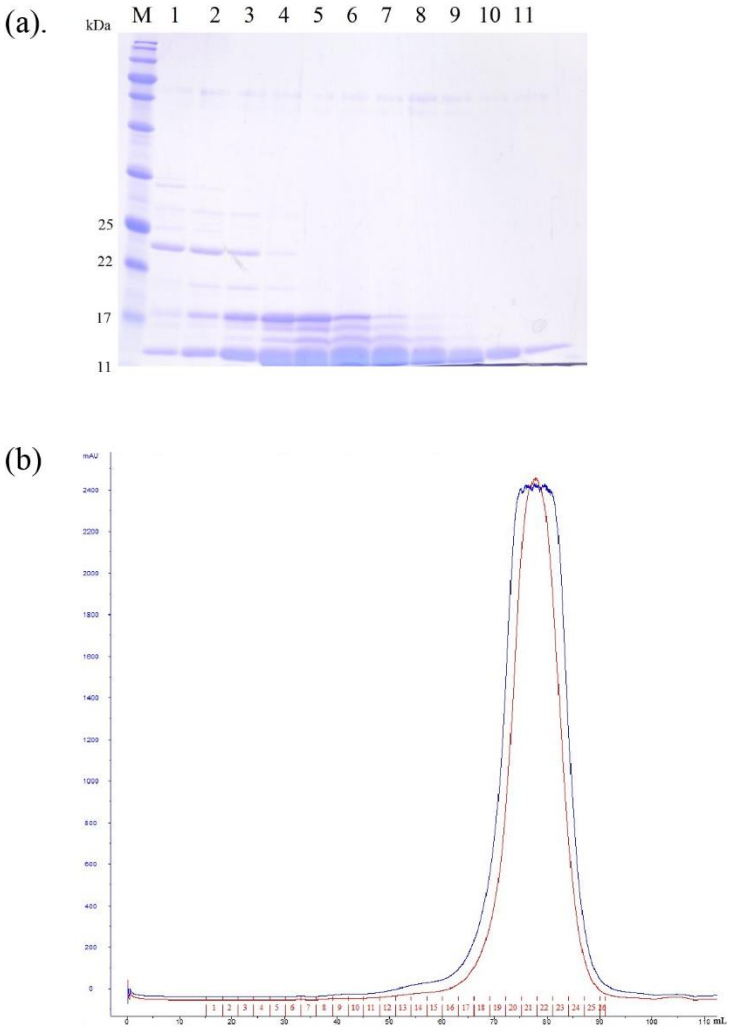

Figure 15 (a) SDS-PAGE and (b) chromatogram of Trx-*f*2 protein purification at size exclusion chromatography step. Lane M, protein marker; lane 1-11, elution 16th-26th fraction. The 19th-26th fractions were collected and concentrated for complex formation.

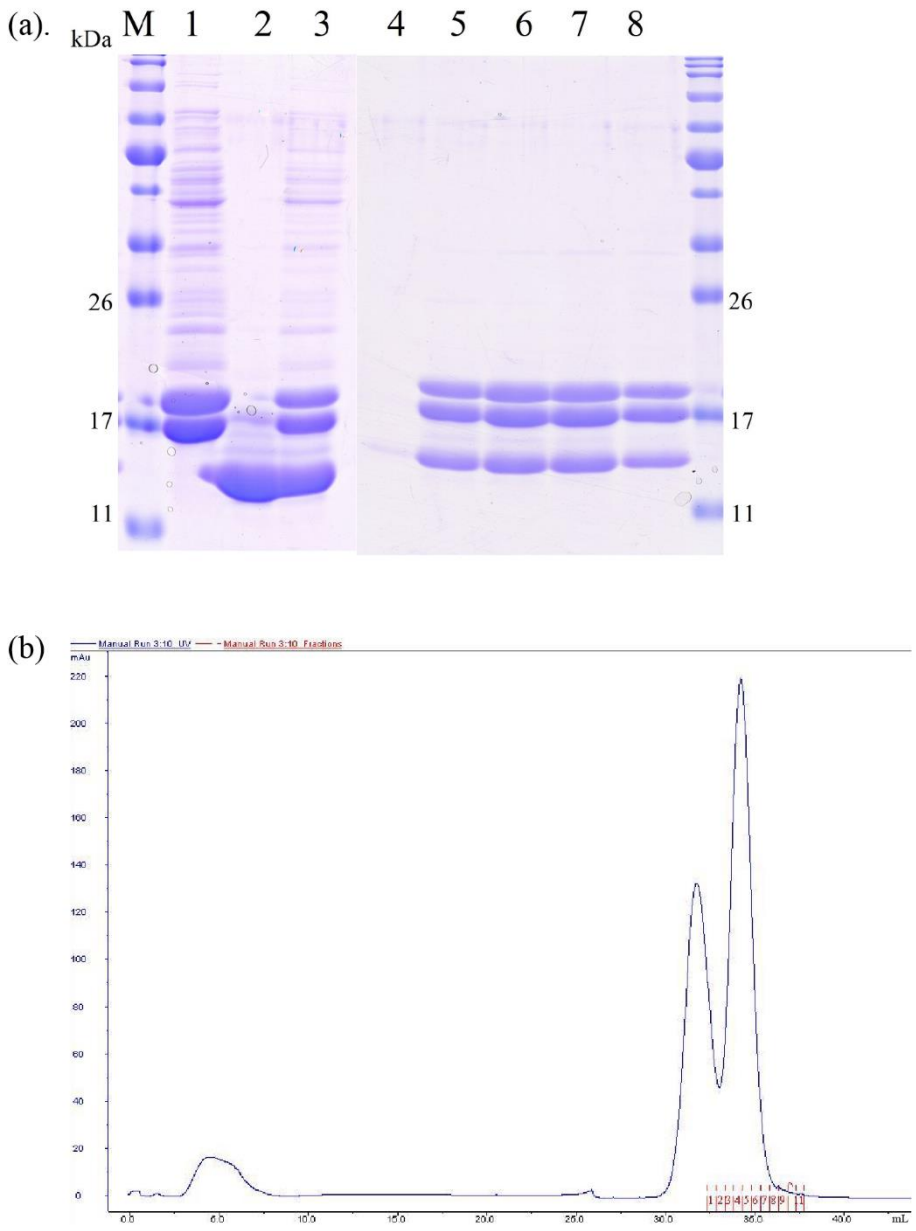

Figure 16 SDS-PAGE and chromatogram of FTR:Trx-*f*2 complex repurification. Lane M, protein marker; lane 1, purified FTR protein; lane2, purified Trx-*f*2 protein; lane 3, the mixture of FTR and Trx-*f*2; lane 4, flow-through; lane 5-8, elution 5^{th}-8^{th} fraction.

Crystallization, data collection, and structure determination

The crystallization trial was carried out by the sitting-drop vapor diffusion method using a commercial crystallization kit at 20 ºC. In the initial screening, plates and needle-like crystals were grown in 0.2 M magnesium nitrate and 20% PEG 3,350. In contrast, needle-like crystals were obtained in 200 mM magnesium chloride, 100 mM Tris-HCl (pH 8.5), and 30% PEG 4,000. Then, the crystals were optimized by changing the concentration of precipitant. The crystals obtained from a condition of 200 mM magnesium nitrate and 16-20% PEG 3,350, as shown in Figure 17 diffracted well when X-ray experiment applied. The orthorhombic crystal was soaked in crystallization buffer with 25% glycerol, flash-cooled, and stored in liquid nitrogen.

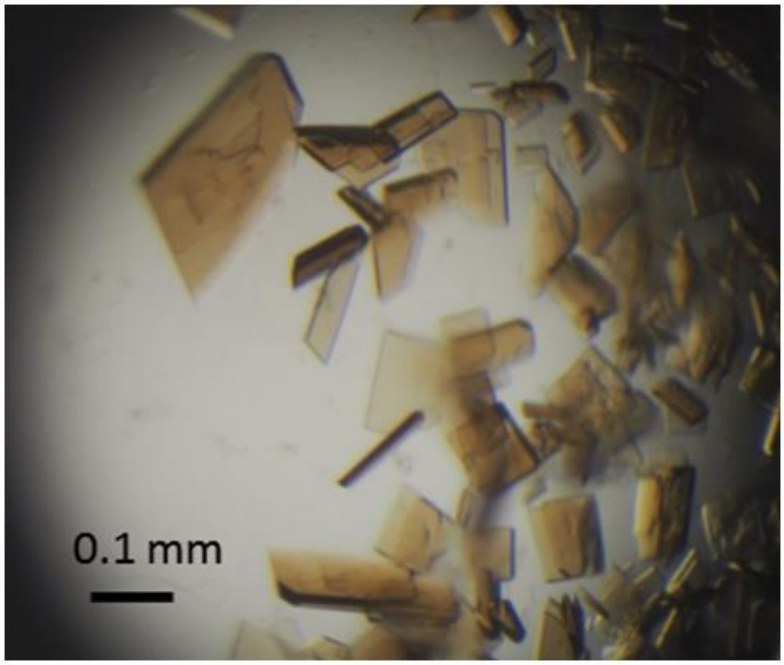

Figure 17 Crystals of FTR:Trx-*f*2.

The X-ray diffraction data were collected at synchrotron beamline BL44XU, SPring-8 (Hyogo, Japan) using EIGER X16M detector (Dectris, Baden, Switzerland). The crystal of FTR:Trx-*f*2 complex belonged to $P2_12_12_1$ with cell parameters of a = 68.74, b = 83.94, c = 69.04 Å. The Matthews coefficient of crystal FTR:Trx-*f*2 was 2.52 $Å^3$/Da with one complex molecule in the crystallographic asymmetry unit and 51% solvent content [34]. The phase was determined by program PHASER in the CCP4 program suite using *Synechocystis* FTR and spinach Trx-*f* (PDB 2PU9) as a search model [35]. The initial model was manually corrected using COOT and refined by PHENIX.refine [36,37]. The data collection and refinement statistics are summarized in Table 2.

Table 2 Data collection and refinement statistics.

Data collection	
Wavelength (Å)	0.9000
Resolution range (Å)	48.71-1.79 (1.90-1.79)
Space group	$P2_12_12_1$
Unit cell	
a, b, c (Å)	68.74, 83.94, 69.04
α, β, γ (º)	90, 90, 90
Total reflections	257225 (42160)
Unique reflections	37812 (5988)
Multiplicity	6.1 (6.3)
Completeness (%)	99.4 (98.6)
Mean I/sigma(I)	13.16 (2.53)
*R-m*erge	0.105 (0.943)
*R-m*eas	0.114 (0.965)
$CC_{1/2}$	0.998 (0.833)
Refinement	
Reflections used in refinement	37802
Reflections used for *R-f*ree	1891
R-work (%)	17.93
*R-f*ree (%)	21.05
Number of non-hydrogen atoms	2773
macromolecules	2470
ligands	65
solvent	238
RMS(bonds) (Å)	0.007
RMS(angles) (º)	0.81
Ramachandran favoured (%)	97.37
Ramachandran allowed (%)	2.63
Ramachandran outliers (%)	0.00
Clashscore	1.39
Average B-*f*actor ($Å^2$)	28.38
macromolecules	27.67
ligands	35.04
solvent	33.94
PDB ID	7C2B

Statistics for the highest-resolution shell are shown in parentheses.

Discussion

The crystal structure of FTR:Trx-*f*2 complex was determined at 1.79 Å resolution. The final model was refined to *R*-work and *R-f*ree of 17.93% and 21.05%, respectively. The FTR:Trx-*f*2 complex contained Trx-*f*2, catalytic, and variable subunit of FTR. The electron density map showed a well-defined and continuous density for residues 3 to 114 of FTRC, residues 24 to 111 of FTRV, and residues 5 to 114 of Trx-*f*2. Residues 1 to 23 in the N-terminal region of FTR variable subunit were invisible. It may be caused by flexibility or cleavage because those N-terminal regions are rich with serine residues implying its structural instability [40]. In the case of spinach FTR, the removal of up to 24 N-terminal residues of the variable subunit stabilizes FTR and does not change any catalytic properties [41].

The overall complex structure of FTR:Trx-*f*2 displayed a similarity to that of *Synechocystis* FTR (ssFTR) and spinach Trx-*f* or -*m*. Trx molecule interacted mostly with FTRC (Figure 18). The structure of FTRC contained five helices that are similar to ssFTRC. On the other hand, the FTRV structure was slightly different from ssFTRV due to a less conserved sequence. FTRV had an open β-barrel structure containing five antiparallel β-sheets similar to ssFTRV but with an extra helix in the N-terminus. Due to length differences of sequence, third and fourth β-sheets of FTRV were longer than those of ssFTRV. Trx-*f*2 retained the overall thioredoxin fold, containing a four-stranded mixed β-sheets, surrounded by four helices. However, the first nine residues at N-terminal were more flexible forming a loop instead of β-strand (β1).

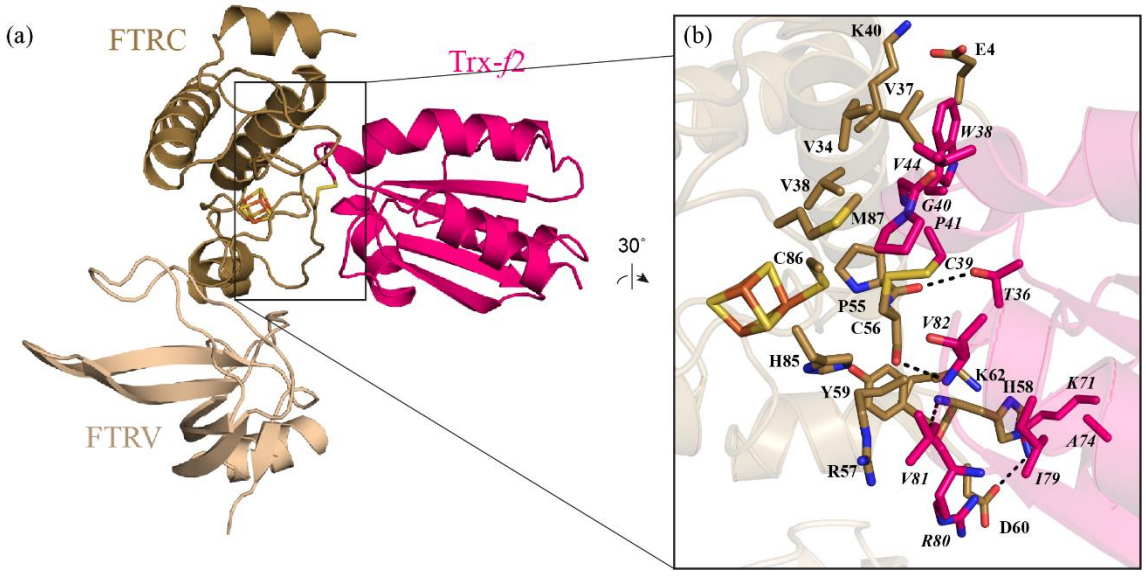

Figure 18 (a) Overall structure of the FTR:Trx-*f*2 complex. Trx-*f*2, catalytic, and variable subunits of FTR are shown in magenta, brown, and light brown, respectively. Trx-*f*2 exclusively interacts with the catalytic subunit of FTR. (b) The interactions between the catalytic subunit of FTR and Trx-*f*2. An intermolecular disulfide bridge between C56 of FTR and C39 of Trx-*f*2 links the active sites of FTR and the Trx shown in yellow stick. Hydrogen bonds are represented as black dashed lines. Labels for amino acids in FTR and Trx are shown in bold and bold italics, respectively.

The important interactions between subunits of ssFTR were made by side chain to side chain hydrogen bonds interaction between E81 and R82 of the catalytic subunit and H64 and E69 of the variable subunit in ssFTR [38]. These interactions were also found in *A. thaliana* FTR structure (between E80, R81 of FTRC and H101, E106 of FTRV). Furthermore, the E80 residue of FTRC also interacted through main chain to main chain

hydrogen bonds with Y47 of FTRV and through hydrophobic interaction with V46, T100, H48 of FTRV whereas side chain R81 of FTRC interacted with main chain H101 of FTRV via hydrogen bonds and with Y47, L44, L80, L102 of FTRV through hydrophobic interaction. Other hydrogen bonds were formed between E65 and W71 of FTRC to S77 of FTRV. Besides this, there were hydrophobic interaction involving, among others, D61, A64, E65, G67, Q68, F70, W71, V76, R79, K82 of FTRC and Y47, H48, W71, K74, I76, S77, A78, N79, L80, E106 of FTRV (Figure 19a).

Trx-*f*2 molecule interacted with the variable subunit of FTR through hydrophobic interaction formed by residue R80 of Trx-*f*2 with residue S77 of FTRV. The FTR:Trx-*f*2 complex was mainly stabilized by an intermolecular disulfide bridge between C39 of Trx-*f*2 with C56 of FTRC and other interactions, shown in Figure 18b and Figure 19b. The interactions between Trx-*f*2 and FTRC concentrated in the center of the molecular surface where the number of hydrophobic interactions formed by residues W38, C39, G40, P41, V44, K71, A74, I79, R80, V81, V82 of Trx-*f*2 with residues E4, V34, V37, V38, K40, G41, P55, C56, R57, H58, Y59, D60, K62, H85, C86, M87 of FTRC. Besides this, there were side chain to side chain hydrogen bonds between K71 of Trx-*f*2 to D60 of FTRC and main chain to main chain hydrogen bonds between T36, R80, V82 of Trx-*f*2 to P55, H58, C56 of FTRC.

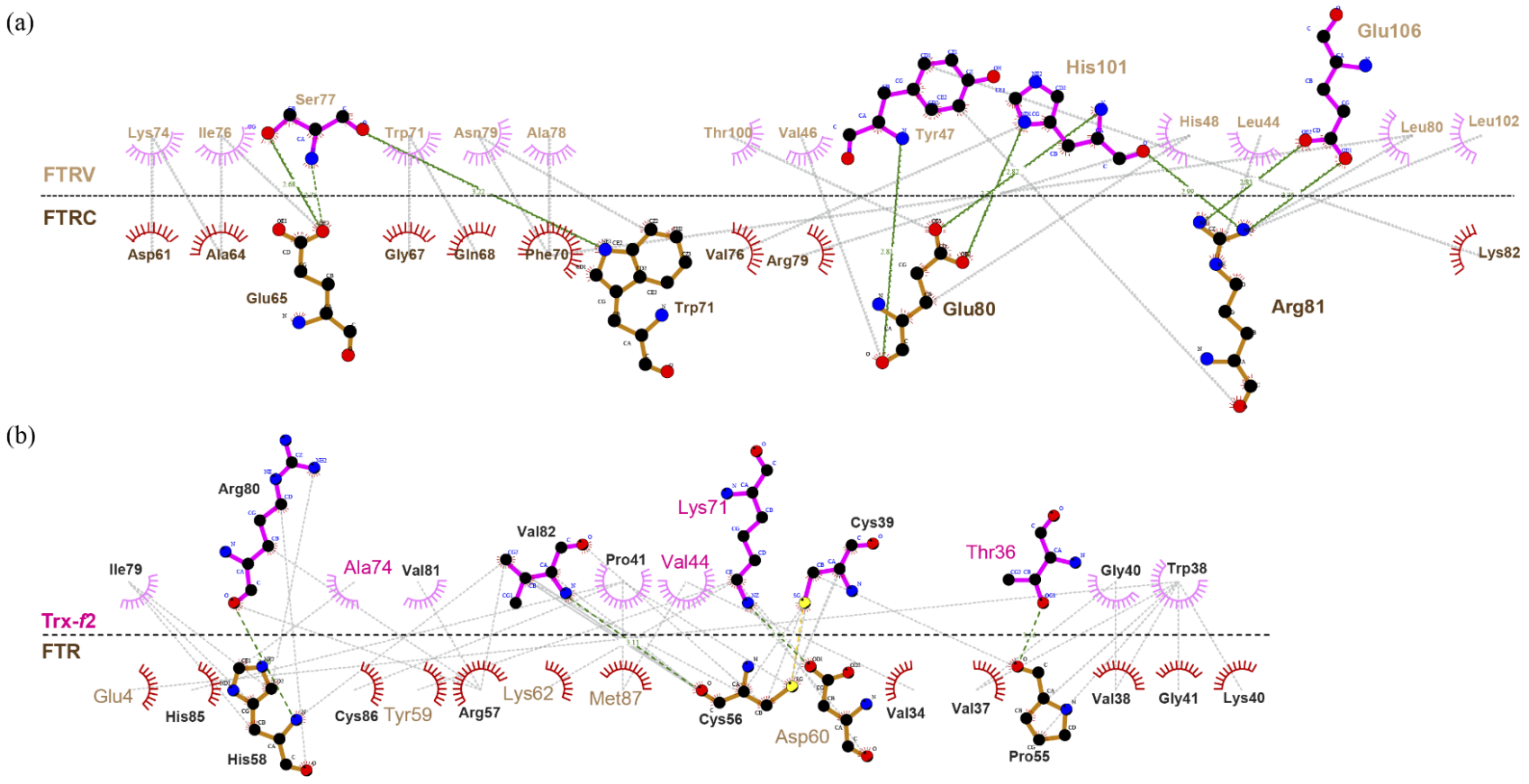

Figure 19 Interaction between catalytic subunit of FTR with (a) variable subunit of FTR and (b) Trx-*f*2. Illustrated by Dimplot in Ligplot+ [33]. Hydrogen bond interaction is shown in green dash and hydrophobic interaction is shown in red dash.

CHAPTER 3

STRUCTURE OF FTR AND TRX-*M*2 PROTEIN COMPLEX

Introduction

As I already introduced in General Introduction, *A. thaliana* has ten Trx isoforms classified into five subtypes (two Trx-*f*, four Trx-*m*, one Trx-*x*, two Trx-*y*, and one Trx-*z*). Trx-*m* is the most abundant isoform among chloroplast Trx enzymes, accounting for up to 70%. The abundance of *m*1 and *m*2 is similar to that of *m*4, while *m*3 is less abundant. Trx-*m* can reduce FBPase in the Calvin-Benson cycle, and NADP-MDH in the tricarboxylic acid cycle. Trx-*m* plays a negative role in redox regulation of kinase STN7, and its overexpression in tobacco weakens the photosynthetic performance. Trx-*m*3 is involved in intracellular protein transportation and meristem maintenance, while Trx-*m*4 affects cyclic electron transport. Trx-*m*1, Trx-*m*2, and Trx-*m*4 act together to regulate PSII biogenesis and xanthophyll cycle [42,43].

Dai *et al.* (2007) has solved the structure of *Synechocystis* FTR with spinach Trx-*m.* Similar to FTR:Trx-*f* complex, Trx-*m* interacted mostly with FTR catalytic subunit. In this chapter, the structure of complex FTR with Trx-*m*2 from *A. thaliana* would be discussed.

Materials and methods

1. Construction and mutation

Mutation C41S was engineered to pET23-a-Trx-*m*2 plasmid (Figure 20) by PCR mutagenesis using PrimeSTAR MAX DNA Polymerase (Takara Bio Inc. CA, USA) with forward primer 5`-ggaccttccaagatgattgatc-3` and reverse primer 5`-catcttggaaggtccacacc-3` (Invitrogen, Thermo Fisher Scientific, Japan). The sequence of mutation plasmids was confirmed by DNA sequencing using BigDye terminator cycle sequencing kit (Applied Biosystem) and ABI 3130 automated DNA sequencer (Applied Biosystem). FTR and Trx:*m*2 from *A. thaliana* were expressed and purified, as previously described in Chapter 1.

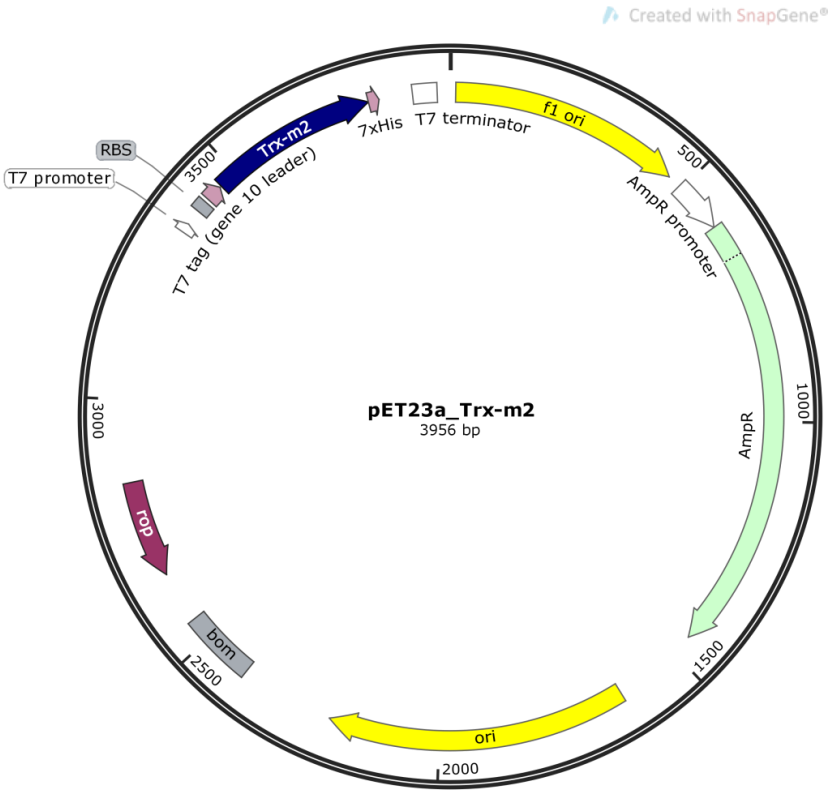

Figure 20 Map of recombinant expression plasmid pET23a-Trx-*m*2. Illustrated by SnapGene viewer (from GSL Biotech; available at www.snapgene.com).

2. Crystallization, data collection, and structure determination

The crystallization trials of FTR:Trx-*m*2 complex were conducted by the sitting-drop vapor diffusion technique using Crystal screen I and II, Peg ion 1 and 2, Peg Rx I and II (Hampton Research, Aliso Viejo, CA, USA), and Wizard I, II, III, and IV (Rigaku, Bainbridge Island, WA, USA) at 4 ^{0}C and 20 ^{0}C, as similar as the case of FTR:Trx-*y*1 or FTR:Trx-*f*2. The sample concentration was 10 mg mL^{-1} of FTR in 25 mM Tris-HCl (pH 7.5). After crystals were obtained in the initial screen, the crystallization conditions were further optimized by the hanging-drop vapor diffusion method using varying the precipitant concentration and pH around the original hit.

The best crystals of FTR:Trx-*m*2 were obtained in 100 mM sodium citrate (pH 6.2) and 18% PEG 3,350 at 4 ^{0}C. After the crystals were grown enough to be checked, the crystal was picked using a loop, briefly soak into the cryoprotectant solution that is crystallization buffer with additional 25% glycerol, and quickly frozen in liquid nitrogen. The crystals were stored in the liquid nitrogen until they are used for X-ray diffraction.

X-ray diffraction data of FTR:Trx-*m*2 were collected with an X-ray of wavelength of 1.0000 Å on beamline TPS 05A at NSRRC (Hsinchu, Taiwan) using CCD detector MX-300HE (Rayonix, Evanston, IL). The diffraction data were collected at 100 K and processed using XDS [30]. The protein structure of FTR:Trx-*m*2 was determined by molecular replacement with program PHASER in the CCP4 program package [31] using *Synechocystis* FTR and mutant spinach Trx-*m* (PDB ID 2PUK) as a search model. The structure of FTR:Trx-*m*2 complex was refined with PHENIX [32]. Figures were prepared using PyMol (The PyMOL Molecular Graphic System, Version 2.0 Schrödinger, LLC), and protein-protein interactions were checked by Dimplot in Ligplot+ [33].

Results

Protein expression and purification

Both FTR and Trx-*m*2 proteins were expressed in *E. coli* BL21 (DE3). The cells were cultured in LB medium at 37 ºC. When the OD_{600} reached 0.5-0.8, the protein expression was induced by 0.5 mM IPTG. The purification of FTR was same as previously described in Chapter 1. The first step of purification of Trx-*m*2 was anion exchange chromatography, and the protein was in the flow-through. The next step was hydrophobic chromatography which was followed by size exclusion chromatography as the final step. Recombinant Trx-*m*2 protein was contained 114 amino acid residues (C73-P186 of At4g03520), and its molecular weight is ~12 kDa on SDS-PAGE (Figure 21). The protein concentration was measured using the molar extinction coefficient, ε_{280} = 21,088 M^{-1} cm^{-1}. Trx-*m*2 was overexpressed with a yield of approximately 39.5 mg per 1-liter culture.

The wild type FTR was mixed with excess mutant Trx-*m*2 in the presence of DTT for complex formation. The mixture was dialyzed and repurified by a combination of cation and anion exchange chromatography to remove the free monomer. The contaminant protein and unreacted Trx-*m*2 was separated from the complex in the flow-through (Figure 22). The fractions which consisted of FTR and Trx-*m*2 proteins were concentrated and filtered in 25 mM Tris-HCl (pH 7.5) for crystallization.

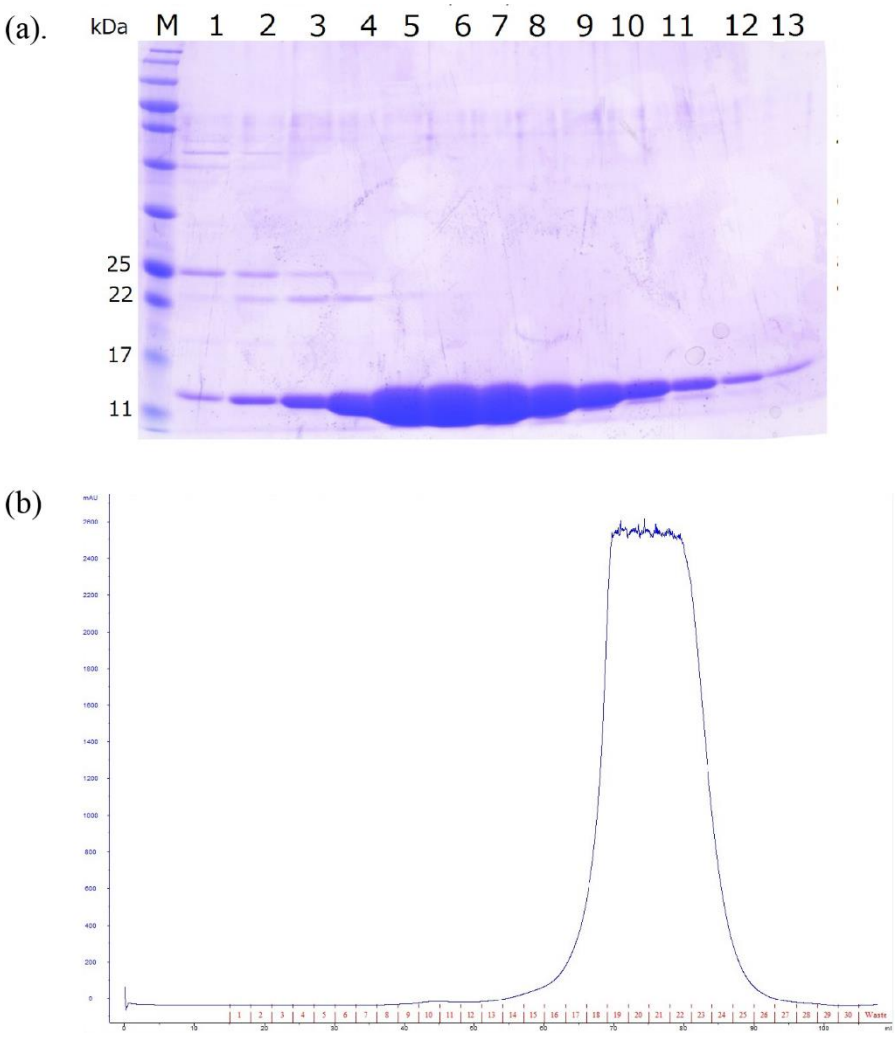

Figure 21 SDS-PAGE and chromatogram of Trx-*m*2 protein at the gel filtration step. Lane M, protein marker; lane 1-13, elution 17th-29th fractions. Fractions from 20 to 28 were collected and concentrated for making FTR:Trx complex.

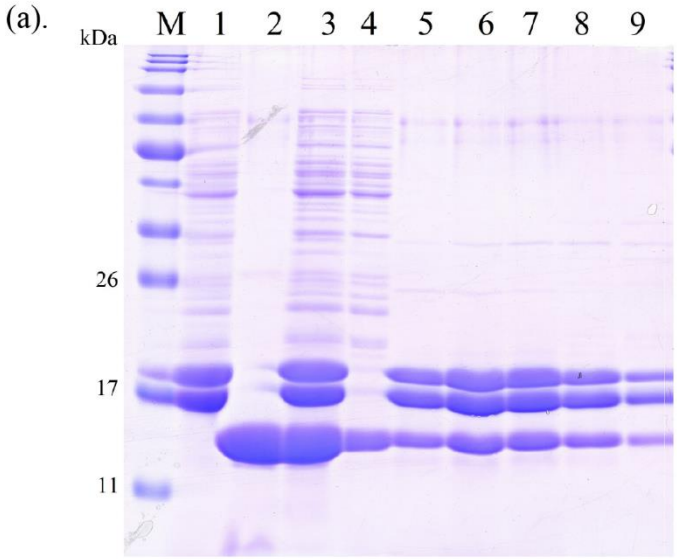

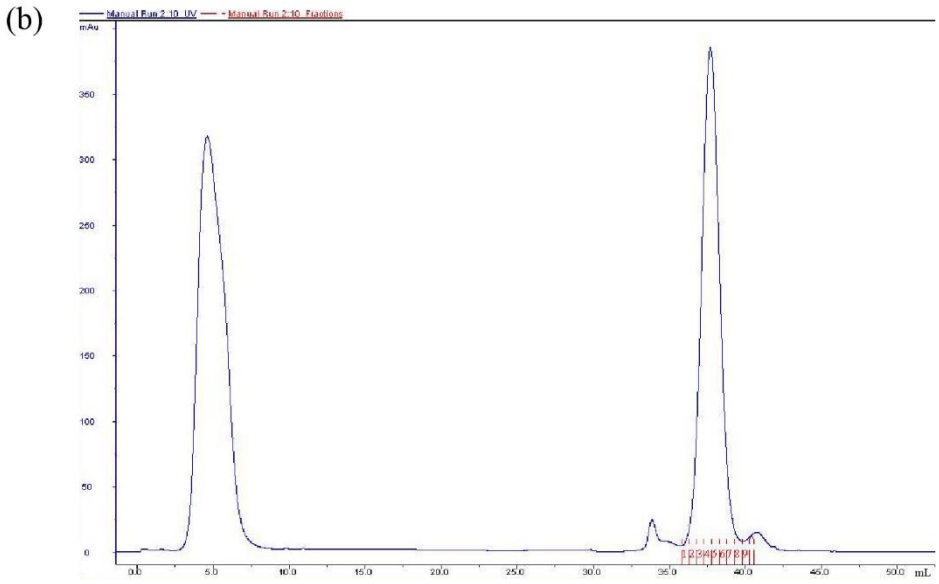

Figure 22 SDS-PAGE and chromatogram of the FTR:Trx-*m*2 complex purification by the ion exchange chromatography. Lane M, protein marker; lane 1, purified FTR protein; lane 2, purified Trx-*m*2 protein; lane 3, the mixture of FTR and Trx-*m*2; lane 4, flow-through; lane 5-9, elution 4^{th}-8^{th} fractions of FTR:Trx-*m*2 complex.

Crystallization, data collection, and structure determination

The FTR:Trx-*m*2 complex with a concentration of FTR around 10 mg mL^{-1} was used for crystallization. The initial screening was performed by the sitting-drop vapor diffusion method using ten commercial kits as similar as in Chapter 1 and 2. In the initial screening, crystals of FTR:Trx-*m*2 were obtained in several conditions and further optimized by the hanging-drop vapor diffusion method. The crystallization conditions were varied around the initial condition by modifying precipitant, precipitant concentration, pH, and addictive reagent. The best crystal of FTR:Trx-*m*2 complex was obtained from droplets comprising 1μL of 10 mg ml^{-1} protein sample and 1μL of reservoir solution containing 100 mM sodium citrate (pH 6.2) and 18% (w/v) PEG 3,350 at 4 ºC (Figure 23).

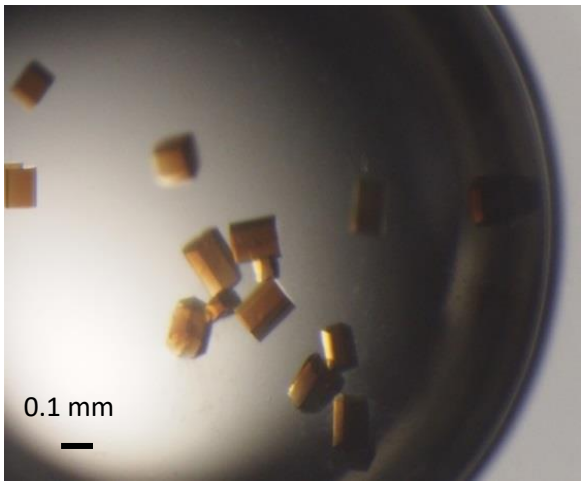

Figure 23 FTR:Trx-*m*2 crystals.

The X-ray diffraction images were collected at synchrotron beamline TPS 05A NSRRC (Hsinchu, Taiwan). The crystal belonged to the monoclinic space group of *C*2, with unit parameters a=174.26, b=137.21, and c=192.46 Å. It was diffracted at 2.4 Å

resolution. The Matthews coefficient was 3.94 $Å^3$/Da, with 71.9% solvent content if there were seven complex molecules of FTR:Trx-*m*2 in the crystallographic asymmetry unit [34]. The self-rotation function was calculated using Molrep in the CCP4 program [44]. There were seven peaks at κ= 180º and one peak at κ= 51.4º, corresponding to non-crystallographic seven-fold symmetry (Figure 24).

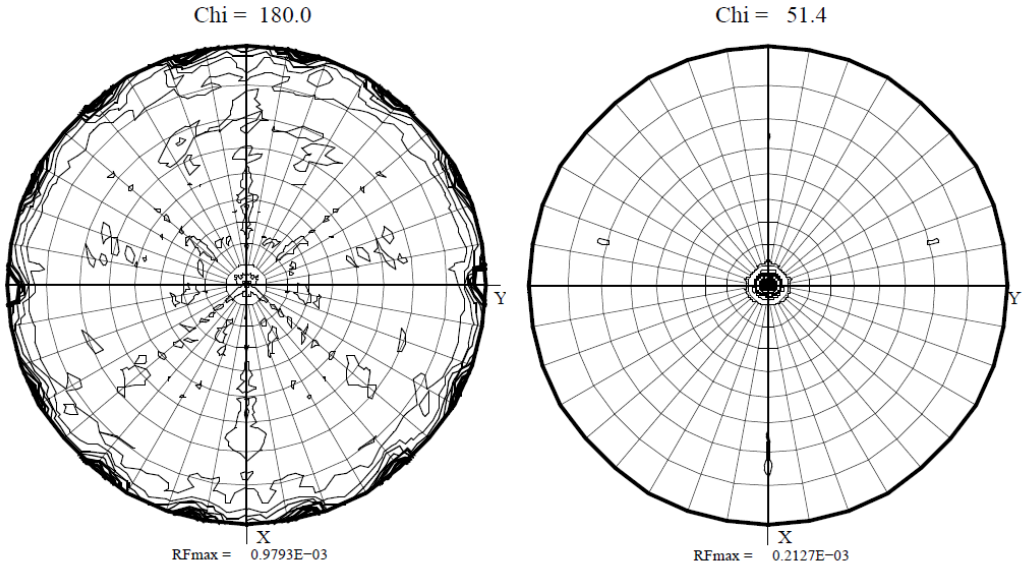

Figure 24 Self-rotation function of FTR:Trx-*m*2 complex at κ= 180 º (left) and 51.4 º (right).

The crystal structure of FTR:Trx-*m*2 was solved by molecular replacement with the program PHASER in the CCP4 program [35] using *Synechocystis* FTR and spinach Trx-*m* (PDB ID 2PUK) as a search model. The model was corrected manually using COOT and refined by PHENIX.refine using NCS restraints [36,37]. There were big positive Fo-Fc density maps during manual refinement, which became an additional complex containing

Trx-*m*2 (chain W) and catalytic subunit of FTR (Chain V). The final values of *R*-work and *R-f*ree were 20.95% and 24.45%, respectively. The data collection and refinement statistics data are listed in Table 3.

Table 3 Data collection and refinement statistics.

Data collection	
Wavelength (Å)	1.0000
Resolution range (Å)	42.52-2.4 (2.54-2.4)
Space group	*C*2
Unit cell	
a, b, c (Å)	174.26, 137.21, 192.46
α, β, γ (º)	90, 90.212, 90
Total reflections	663199 (105966)
Unique reflections	175399 (27733)
Multiplicity	6.2 (6.3)
Completeness (%)	99.14 (96.86)
Mean I/sigma(I)	8.82 (1.31)
*R-m*erge	0.123 (1.285)
*R-m*eas	0.144 (1.494)
$CC_{1/2}$	0.995 (0.539)
Refinement	
Reflections used in refinement	175276
Reflections used for *R-f*ree	8764
R-work (%)	20.95
*R-f*ree (%)	24.45
Number of non-hydrogen atoms	18993
macromolecules	18397
ligands	66
solvent	530
RMS(bonds) (Å)	0.013
RMS(angles) (º)	1.04
Ramachandran favoured (%)	98.76
Ramachandran allowed (%)	1.06
Ramachandran outliers (%)	0.18
Clashscore	7.78
Average B-*f*actor ($Å^2$)	67.22
macromolecules	67.64
ligands	46.26
solvent	55.32
PDB ID	7C3F

Statistics for the highest-resolution shell are shown in parentheses.

Discussion

The crystal structure of the complex between FTR with mutant C41S Trx-*m*2 comprised seven complexes in the crystallographic asymmetry unit. The r.m.s.d. values based on Cα atom among the seven monomer was 0.126-0.293. The recombinant proteins of Trx-*m*2, catalytic, and variable subunit of FTR have 114, 115, and 112 amino acid residues, respectively. The crystal structure of each Trx-*m*2 missed the first 6-7 residues at N-terminal and the last residue at C-terminal, those of each FTRC lost the first or second residues at N-terminal, and those of each FTRV missed the first 22-23 residues at N-terminal and the last residue at C-terminal. As similar as in the case of FTR:Trx-*f*2 structure, residues 1 to 21-22 in the N-terminal region of FTR variable subunit were missed in FTR:Trx-*m*2 complex structures. It may be caused by flexibility or cleavage because those N-terminal regions are rich with serine residues, implying its structural instability [40].

During refinement, there was a big blob of positive Fo-Fc which turned out to be an additional complex between FTRC and Trx-*m*2. This complex had a poor electron density map and I could model only 10-112 residues and some missing parts of the chain. The r.m.s.d. value of this last FTRC and Trx-m2 complex based on the Cα atom was 1.428 Å which was higher than others. This complex may be trapped in the crystal because it is not tightly packed with 71.9% solvent. I will use chains A, B and C to describe the structure of the FTR:Trx-*m*2 complex because their electron density map is better than the others.

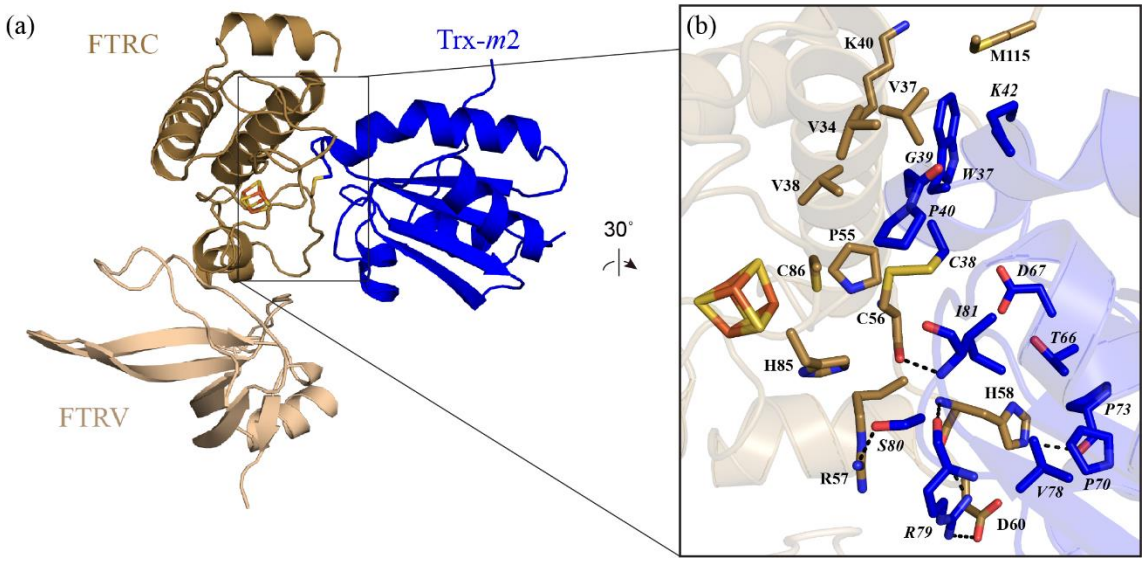

Figure 25 (a) Overall structure of the FTR:Trx-*m*2 complex. Trx-*m*2, catalytic, and variable subunits of FTR are shown in blue, brown, and light brown, respectively. Trx-*m*2 exclusively interacts with the catalytic subunit of FTR. (b) The interactions between the catalytic subunit of FTR and Trx-*m*2. The iron-sulfur cluster and disulfide bridge between C56 of FTR and C38 of Trx-*m*2 are shown in yellow-orange and yellow sticks, respectively. Hydrogen bonds are represented as black dash. Labels for amino acids in FTR and Trx are shown in bold and bold italics, respectively.

The overall structure of FTR:Trx-*m*2 showed a similarity to those of FTR:Trx-*f*2. Trx-*m*2 had a four-stranded mixed β-sheets, surrounded by four helices maintaining thioredoxin fold. The first eight residues at N-terminal were flexible, forming a loop instead of β-strand (β1). FTRC structure was similar to *Synechocystis* FTRC composing of five helices with an iron-sulfur cluster and the redox-active Cys residues. The structure of FTRV

was also similar to that of *Synechocystis* FTRV containing five antiparallels β-sheets with an additional α-helix at N-terminal (Figure 25a).

The FTR:Trx-*m*2 complex was stabilized by an intermolecular disulfide bridge (C56 of FTRC and C38 of Trx-*m*2) and the number of interactions at the interface, as displayed in Figure 25b and Figure 26. Trx-*m*2 interacted with FTRV through hydrophobic interaction of R79 of Trx-*m*2 and S78 of FTRV but mostly with FTRC. The side chain R57, D60 of FTRC formed hydrogen bond interactions to the side chain S80, R79 of Trx-*m*2. The carbonyl oxygen C56 of FTRC interacted through hydrogen bonds to the amide nitrogen I81 of Trx-*m*2. The residue H58 formed interaction with P70 and R79 through hydrogen bond. In addition to that, the hydrophobic interactions were involved, among others, E4, V34, V37, V38, K40, G41, P55, C56, R57, H58, D60, H85, C86, M115 of FTRC and W37, C38, G39, P40, K42, T66, P70, P73, V78, A79, S80, I81 of Trx-*m*2 (Figure 26).

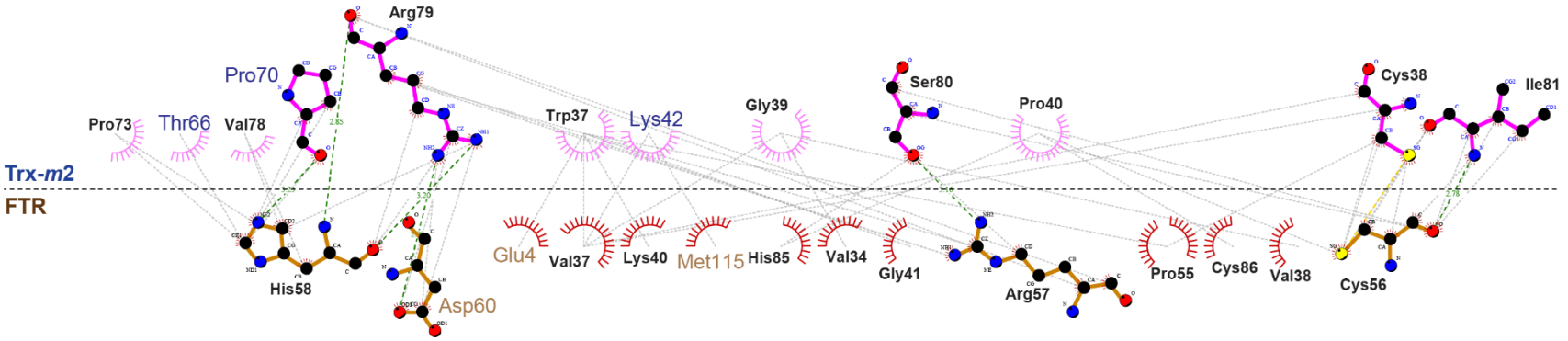

Figure 26 Interaction between catalytic subunit of FTR with Trx-*m*2. Illustrated by Dimplot in Ligplot+ [33]. Hydrogen bond interaction is shown in green dash and hydrophobic interaction is shown in red dash.

CHAPTER 4

STRUCTURE ANALYSIS OF FTR AND TRXS IN NON-COMPLEXED FORM

Introduction

The *A. thaliana* genome encoded ten different Trx isoforms targeted to chloroplasts [20]. In the previous chapters, I have determined three FTR:Trx complexes. The crystal structures of the complex between *A. thaliana* FTR and Trx representatives from each class have been determined at 1.59 Å resolution for FTR:Trx-*y*1 (in Chapter 1, high group), 1.79 Å resolution for FTR:Trx-*f*2 (in Chapter 2, middle group) and 2.4 Å resolution for FTR:Trx-*m*2 (in Chapter 3, low group).

To date, the crystal structures of the complex between *Synechocystis* FTR and spinach Trx-*f* (PDB ID 2PU9) or -*m* (PDB ID 2PUK) have been determined [23]. However, no native structure of FTR or Trx isoforms from *Arabidopsis* have been published before. It was difficult to compare the structure of FTR or Trx before complex formation. In this chapter, I tried to solve the structure of FTR or Trx isoforms alone from *Arabidopsis* at the resolution high enough to provide the information on the structural changes of side chain conformations upon complex formation which might be crucial to provide different affinity of FTR to Trx isoforms, suggesting the structural basis for the Trx isoform-based fine-tuning mechanism of FTR activity.

Materials and methods

1. Preparation of proteins

Plasmids of wild type FTR, mutant C40S Trx-*m*1 and C33S Trx-*y*2 were provided by my collaborator, Hisabori-Wakabayashi Laboratory, Tokyo Institute of Technology Japan. The recombinant proteins of FTR, Trx-*m*1 and Trx-*y*2 from *A. thaliana* were expressed and purified, as previously described in Chapter 1.

2. Crystallization

The crystallization trial of FTR, Trx-*m*1 and Trx-*y*2 was carried out by the sitting-drop vapor diffusion at 4 ^{0}C and 20 ^{0}C. I used commercial screening kits: Crystal screen I and II, Peg ion 1 and 2, Peg Rx I and II (Hampton Research, Aliso Viejo, CA, USA), and Wizard I, II, III, and IV (Rigaku, Bainbridge Island, WA, USA) and the crystallization robot, Mosquito LCP (TTP Labtech). The concentration of the crystallization sample was 10 mg mL^{-1} in 25 mM Tris-HCl (pH 7.5).

2.1 3D crystal of FTR and Trx-*y*2

After initial screening, the crystallization was conducted by hanging-drop vapor diffusion and the conditions were optimized by changing the buffer, pH, precipitant, and additives. I used 10 mg mL^{-1} of FTR for initial screening and optimization of crystallization. The sample buffer consisted of 25 mM Tris-HCl (pH 7.5). The droplet was contained 1 µL FTR and 1 µL reservoir solution, then equilibrated with 150 µL reservoir solution at 4 ºC and 20 ºC. The crystal was picked up using the loop and soaked into cryoprotectant composed of crystallization buffer and 25% glycerol. The crystal was briefly frozen in liquid nitrogen and store in cryo condition.

In the initial screening, the crystals of Trx-*y*2 only grew in crystallization buffer consisting of 0.2 M Sodium Citrate, 0.1 M sodium cacodylate (pH6.5), 30% 2-propanol at 4 ^{0}C. The crystallization condition was further optimized by changing the concentration of the protein and 2-propanol. The crystal was soaked into cryoprotectant containing crystallization buffer and 30% glycerol and flash-cooled in liquid nitrogen.

The FTR and Trx-*y*2 crystals were checked at a wavelength of 0.9000 and 0.8000 Å, respectively, on beamline BL44XU at SPring-8 (Hyogo, Japan) using EIGER X16M detector (Dectris, Baden, Switzerland).

2.2 Crystal structure of Trx-*m*1

In the crystallization trial, the good crystals of Trx-*m*1 were obtained in 100 mM HEPES (pH 7.5), 10% 2-propanol, and 20% PEG 4,000 20 ^{0}C. After the crystals were grown enough to be checked, the crystal was picked using a loop, briefly soak into the cryoprotectant solution composing crystallization buffer with additional 15% glycerol, and quickly frozen in liquid nitrogen. The crystals were stored in the liquid nitrogen until they are used for X-ray diffraction.

X-ray diffraction images of Trx-*m*1 were collected using an X-ray of a wavelength of 0.9000 Å on beamline BL44XU at SPring-8 (Hyogo, Japan). The diffraction data were collected at 100 K and processed using XDS [30]. The protein structure was determined by molecular replacement with program PHASER in the CCP4 program package [31] using mutant spinach Trx-*m* (PDB ID 2PUK) as a search model. The structure of Trx-*m*1 protein was refined with SHELXL [45].

3. Structural comparison between FTR or Trx in the complex and non-complex form

I superposed *Synechocystis* FTR (PDB ID 1DJ7) with *A. thaliana* FTR from three complexes. The monomer of Trx, Trx-*m*1 and spinach Trx-*f* (PDB ID 1FAA), were superposed with Trx-*m*2 and Trx-*f*2 from the FTR:Trx complex, respectively, using CCP4 superposition secondary structure matching of whole chain Trx [46].

Results

3D crystal of FTR

The results of FTR expression and purification were same as described in Chapter 1. The best crystal of FTR was obtained in the drop containing 0.1 M CAPS (pH10.5), 0.2 M $LiSO_4$, 0.8 M NaH_2PO_4, 1.4 M K_2HPO_4 at 20 ^{0}C, as displayed in Figure 27 (*top*). Then, I checked the diffraction pattern from the crystal at SPring-8 BL44XU (Hyogo, Japan).

The FTR crystal was diffracted at 3.0 Å, as displayed in Figure 27 (*bottom*). I processed the diffraction images using XDS [30]. The crystal belonged to *I*422 space group with unit cell parameters of a = 270.6, b = 270.6, and c = 71.4 Å, α = β = γ = 90 º. The completeness of data was 99.9%, I/I(σ) of 7.03, $CC_{1/2}$ of 0.994 and *R*-meas of 27.0% (Table 4). I tried to make the initial model using program PHASER in the CCP4 program suite [35] with *Synechocystis* FTR (PDB ID 1DJ7) and *A. thaliana* FTR from the complex. However, the initial model was not correct. I tried to use several differrent parameters in the molecular replacement calculations and change the estimated number of molecules in the crystallographic asymmetric unit, but I could not determine the correct rotational and translational parameters of molecular replacement for the structure of the FTR monomer.

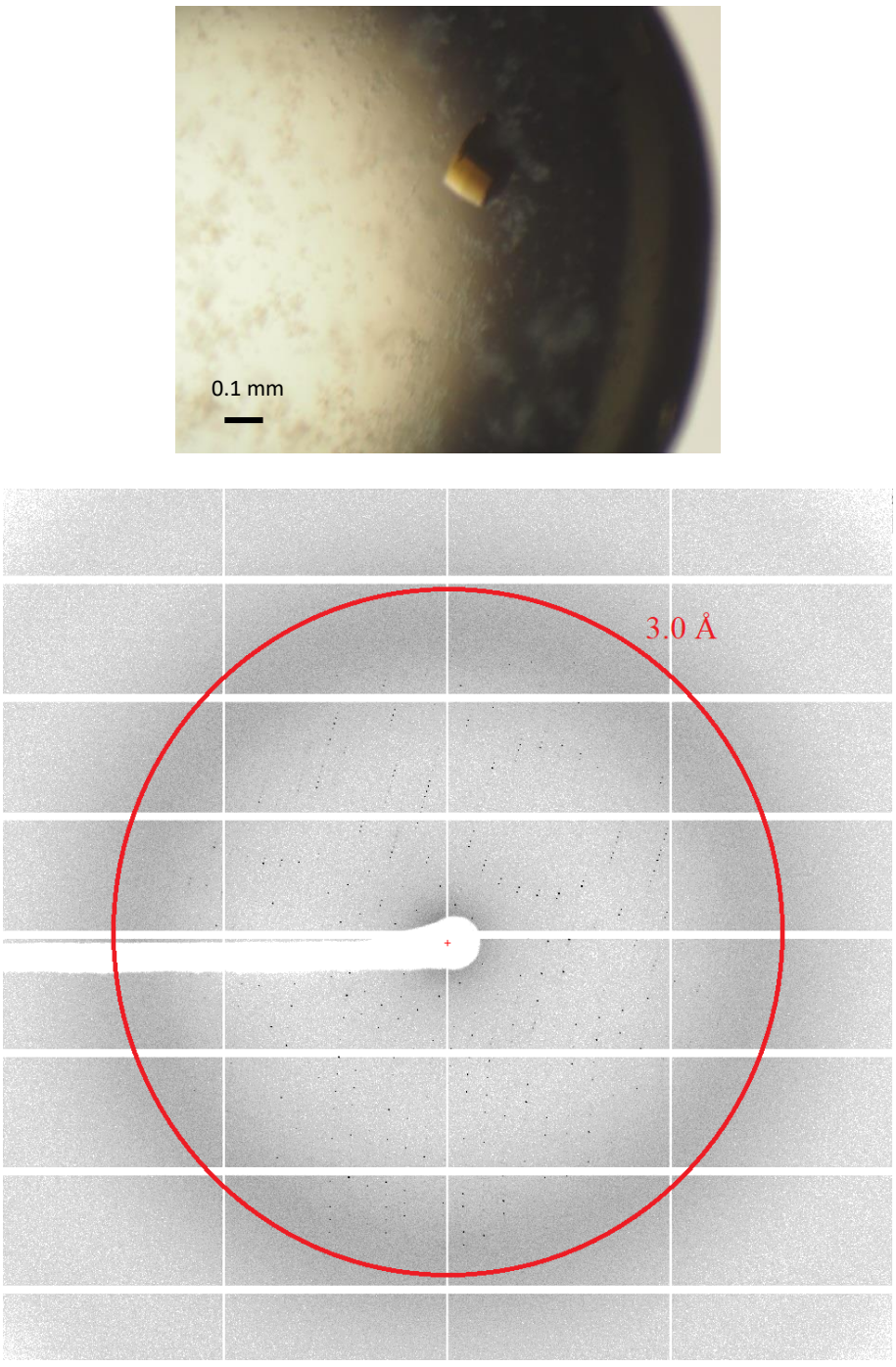

Figure 27 3D crystals (*top*) and diffraction image (*bottom*) of FTR crystal recorded at SPring-8 BL44XU (Hyogo, Japan). The resolution limit is up to 3.0 Å.

Table 4 Crystallographic data of FTR crystal

Data collection	
Wavelength (Å)	0.9000
Resolution range (Å)	48.42-3.00 (3.19-3.00)
Space group	$I4_122$
Unit cell	
a, b, c (Å)	270.6, 270.6, 71.4
α, β, γ (º)	90, 90, 90
Total reflections	319319 (57750)
Unique reflections	26929 (4244)
Multiplicity	5.5 (6.3)
Completeness (%)	99.9 (99.5)
Mean I/sigma(I)	7.03 (1.61)
*R-m*erge	0.26 (1.59)
*R-m*eas	0.27 (1.65)
$CC_{1/2}$	0.994 (0.605)

Crystallization of Trx-*y*2

The recombinant plasmid of Trx-*y*2 was used to transform *E. coli* BL21 (DE3) and cultured in LB medium. The protein expression was induced by 0.5 mM IPTG and the recombinant protein was purified successfully. Recombinant Trx-*y*2 was comprised of 106 amino acids and its molecular weight is around 12 kDa on SDS-PAGE in Figure 28. The protein concentration was measured using the extinction coefficient, ε_{280} = 15,470 M^{-1} cm^{-1}. The yield of Trx-*y*2 after purification was approximately 4.3 mg per 1-liter culture.

I used 10 mg mL^{-1} of Trx-*y*2 in 25 mM Tris-HCl (pH 7.5) for crystallization trials. Initial crystallization screening was performed by the sitting-drop vapor diffusion method using ten commercial screening kits. Initial crystal was obtained in the condition containing 0.2 M Sodium Citrate, 0.1 M sodium cacodylate (pH6.5), 30% 2-propanol at 4 ^{0}C. The initial crystallization condition was optimized by changing the concentration of protein and 2-propanol using the hanging-drop vapor diffusion method. The best crystals were obtained

from the droplet consisted of 1 µL protein (17 mg mL^{-1}) and 1 µL reservoir buffer (0.2 M Sodium Citrate, 0.1 M sodium cacodylate (pH6.5), 30.6% 2-propanol), as shown in Figure 29 (*top*).

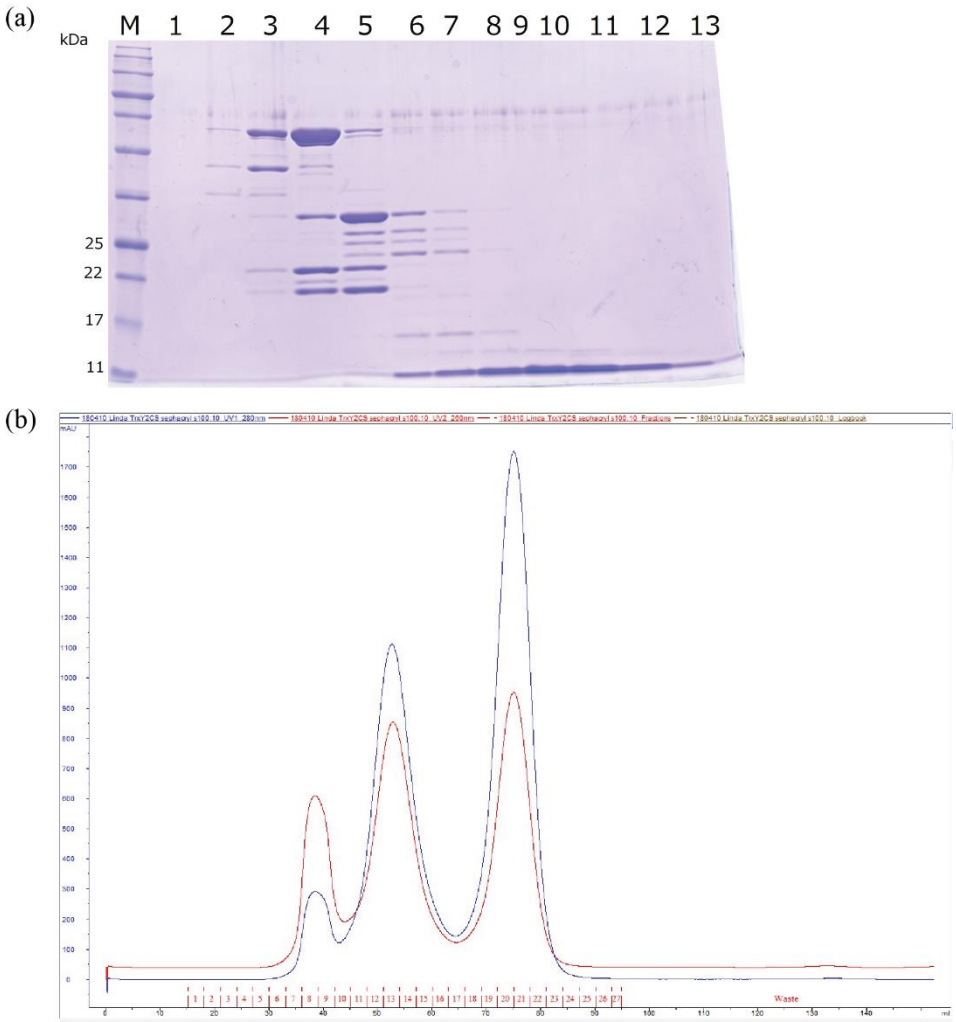

Figure 28 SDS-PAGE and the chromatogram of Trx-*y*2 protein at the last step of purification; Lane M, protein marker; lane 1-2, 7th, 9th fractions (first peak); lane 3-5, 11th, 13th, 15th fractions (second peak); lane 6-13, 17th-24th fractions (third peak). The fractions 19th-24th were collected and concentrated for crystallization.

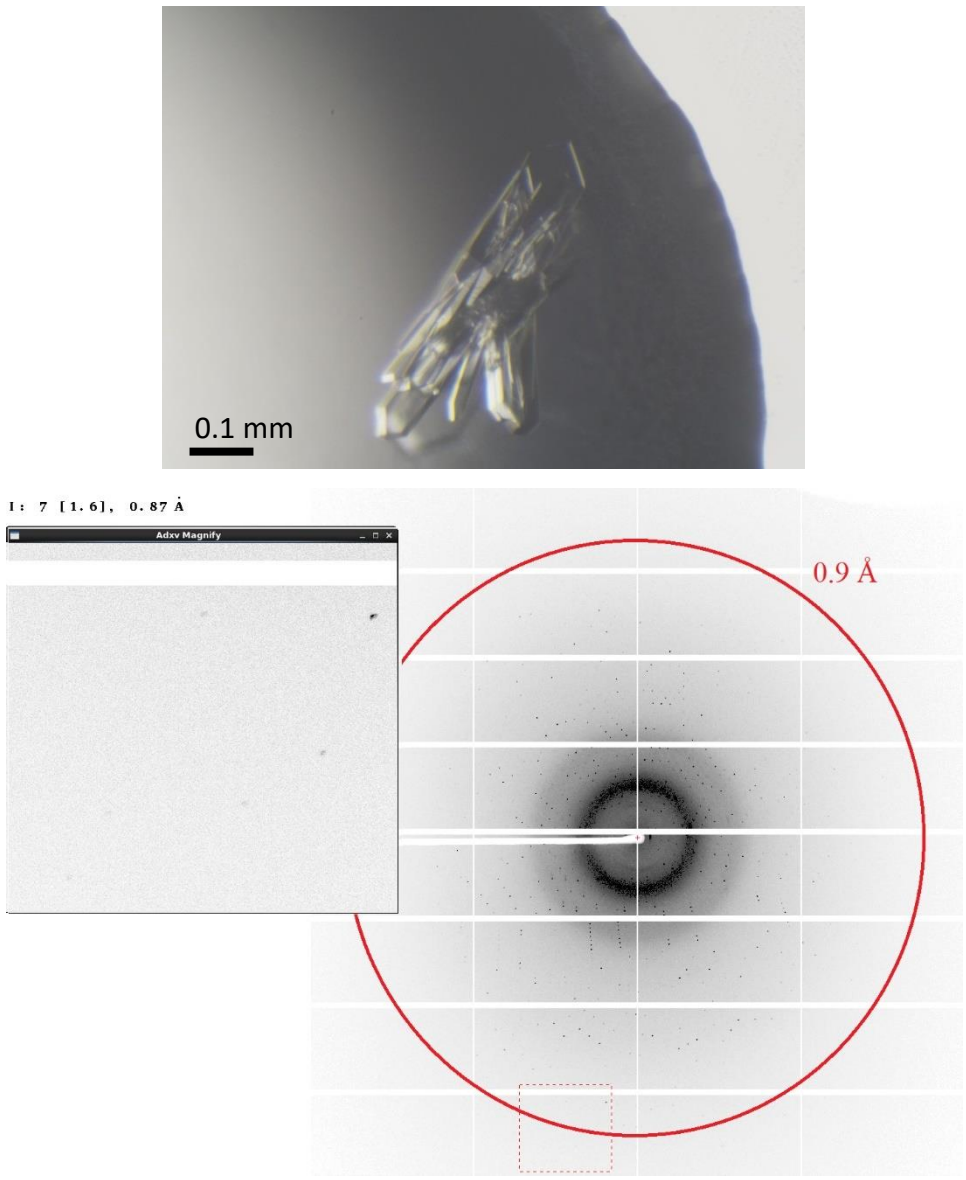

Figure 29 3D crystals (*top*) and a diffraction image (*bottom*) of Trx-*y*2 crystal recorded at SPring-8 BL44XU (Hyogo, Japan). The resolution limit is up to 0.87 Å.

Crystal Structure analysis of Trx-y2 crystal

The Trx-*y*2 crystal was diffracted well up to 0.87 Å and it belonged to *C*222 space group (Figure 29 *bottom*). The data collection was summarized in Table 5. The unit cell parameters were a = 36.7, b = 106.9, c = 37.7 Å, α = β = γ = 90 º. The completeness of data was 99.7%, I/I(sigma) of 10.99, $CC_{1/2}$ of 0.997 and *R*-meas of 12.0%. I did molecular replacement using PHASER program in the CCP4 program suite [35] using the Trx-*y*1 structure as a search model. Unfortunately, I could not get the initial phase angles because the cell volume was too small for the molecule. Therefore, I tried to do molecular replacement using truncated Trx-*y*1 as a search model and got the same results. Since the crystal was diffracted at high resolution, I tried the direct method for phasing problem using SHELXS. I did not succeed in getting the initial phase angles. I have checked the Trx-*y*2 crystal by SDS-PAGE to confirm the crystal was Trx-*y*2 protein (Figure 30).

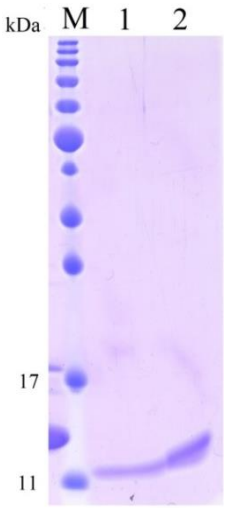

Figure 30 SDS-PAGE of Trx-*y*2 protein; Lane M, protein marker; lane 1, Trx-y2 crystal; line 2, Trx-y2 crystallization sample.

Table 5 Crystallographic data of Trx-*y*2 crystal

Data collection	
Wavelength (Å)	0.8000
Resolution range (Å)	37.72-0.93 (0.98-0.93)
Space group	$C222_1$
Unit cell	
a, b, c (Å)	36.70, 106.90, 37.70
α, β, γ (º)	90, 90, 90
Total reflections	313182 (48909)
Unique reflections	50674 (8036)
Multiplicity	6.4 (6.3)
Completeness (%)	99.7 (98.8)
Mean I/sigma(I)	10.99 (1.61)
*R-m*erge	0.11 (1.12)
*R-m*eas	0.12 (1.23)
$CC_{1/2}$	0.997 (0.890)

Crystals of Trx-*m*1

The recombinant plasmid of Trx-*m*1 was used to transform *E. coli* BL21 and cultured in LB medium until OD_{600} 0.5-0.8. The protein expression was induced by 0.5 mM IPTG at 21ºC for 16-18 hours. The cells were disrupted by sonication using BRANSON 450 Sonifire and the lysate was clarified by centrifugation. The supernatant was applied to the anion exchange chromatography column. The protein eluted in the flow-through and wash fractions. Then the protein was further purified by hydrophobic chromatography and gel filtration column. The purity of protein fraction was confirmed by SDS-PAGE shown in Figure 31. The protein concentration was calculated using the extinction coefficient (ε_{280} = 21,095 M^{-1} cm^{-1}). The Trx-*m*1 protein was overexpressed with a yield of 68 mg per 1-liter culture.

The sample concentration for crystallization was 10 mg mL^{-1} in 25 mM Tris-HCl (pH 7.5). The droplets containing the mixture of 0.2 µL protein complex with 0.2 µL reservoir solution were equilibrated with 80 µL reservoir at 4 ºC and 20 ºC. The good crystal was obtained from the crystallization buffer containing 0.1 M HEPES (pH 7.5), 10% 2-propanol, and 20% PEG 4,000 at 20 ºC (Figure 32). The crystal was picked up and briefly soaked into cryoprotectant buffer containing crystallization buffer and 15% glycerol. Then, the crystal was flash-cooled and stored in liquid nitrogen.

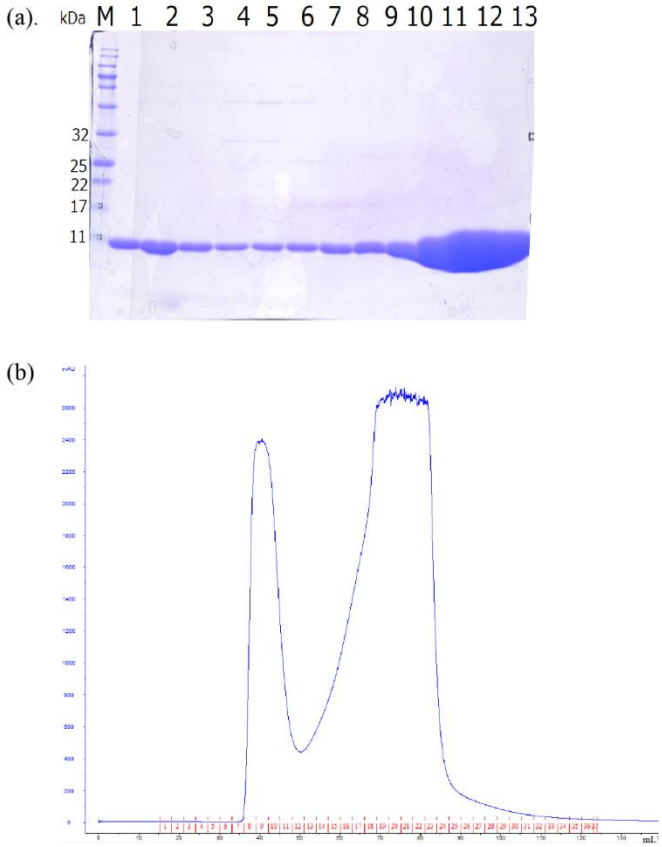

Figure 31 SDS-PAGE and a chromatogram of Trx-*m*1 protein at the size exclusion chromatography step; Lane M, protein marker; lane 1-13, elution 4^{th}-8^{th} fractions. The fractions at the first and second peaks were separately collected and concentrated for crystallization.

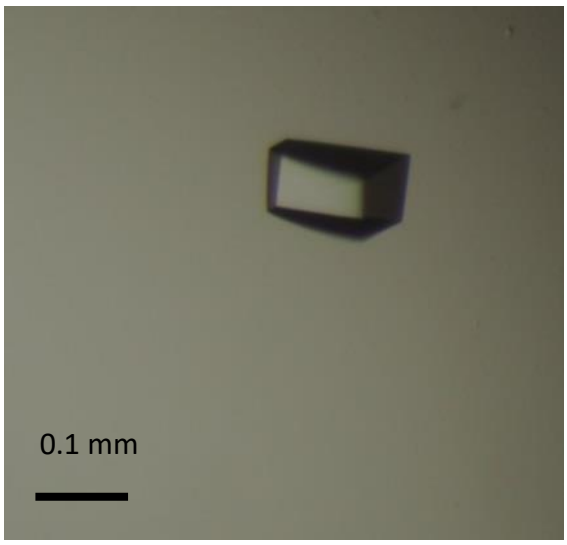

Figure 32 The good crystal of Trx-*m*1 from initial screening at 20 ºC.

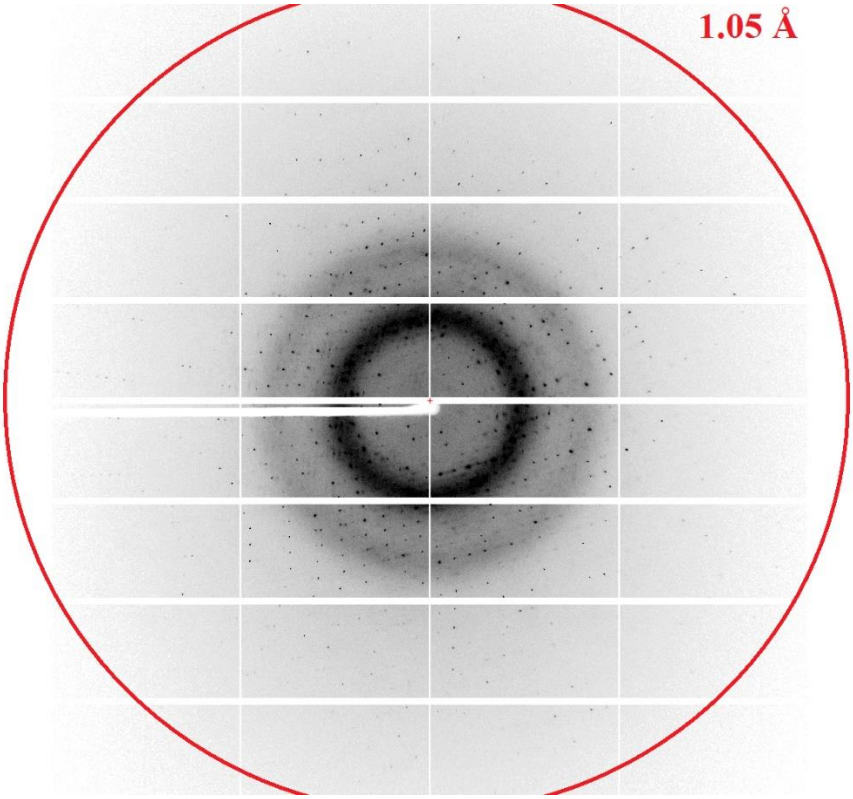

Figure 33 Diffraction image of Trx-*m*1 crystal recorded at SPring-8 BL44XU (Hyogo, Japan). The resolution limit is up to 1.05 Å.

Crystal structure analysis of Trx-*m*1

X-ray diffraction images were collected at synchrotron beamline BL44XU, SPring-8 (Hyogo, Japan). The crystal was diffracted to 1.05 Å resolution and belonged to $P2_1$ space group (Figure 33). The Matthews coefficient was 1.87 $Å^3$/Da for one molecule in the crystallographic asymmetric unit and the solvent prediction was 34.2 % solvent [34]. The initial phase was determined by molecular replacement with program PHASER in the CCP4 program suite [35] using spinach Trx-*m* structure (PDB ID 2PUK) as a search model. The initial model was rebuilt using COOT and refined by SHELXL [36,45]. The data collection and refinement statistics are summarized in Table 6.

Table 6 Data collection and refinement statistics.

Data collection	
Wavelength (Å)	0.9000
Resolution range (Å)	26.68-1.10 (1.13-1.10)
Space group	$P2_1$
Unit cell	
a, b, c (Å)	24.01, 64.33, 29.49
α, β, γ (º)	90, 96.01, 90
Total reflections	238324 (38607)
Unique reflections	35880 (5726)
Multiplicity	6.2 (6.3)
Completeness (%)	99.69 (98.70)
Mean I/sigma(I)	20.98 (9.8)
*R-m*erge	0.058 (0.252)
*R-m*eas	0.063 (0.274)
$CC_{1/2}$	0.998 (0.98)
Refinement	
Reflections used in refinement	35799
Reflections used for *R-f*ree	1668
R-work (%)	14.37
*R-f*ree (%)	18.77
RMS(bonds) (Å)	0.0135
RMS(angles) (º)	2.21
PDB ID	7C65

Statistics for the highest-resolution shell are shown in parentheses.

The electron density map was very clear and shows a continuous density for a polypeptide from residues 4 to 109. The structure was solved at 1.1 Å resolution which is good enough to see some hydrogen atoms and the alternative conformations of the residue. The values of *R*-work and *R-f*ree were 14.37% and 18.77%, respectively. The overall structure of monomeric Trx-*m*1 showed similarity to those of other Trxs in this study: Trx-*y*1, Trx-*f*2 and Trx-*m*2. Trx-*m*1 had an open β- barrel containing mixed β-sheet flanked by four helices maintaining Trx fold, as shown in Figure 34.

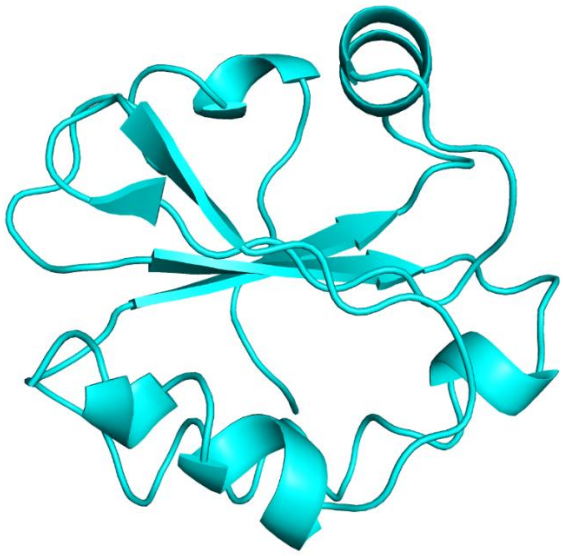

Figure 34 The overall structure of Trx-*m*1.

Discussion

Structural changes of FTR upon complex formation

Sequence alignment of the catalytic subunit of FTR from *A. thaliana* (*At*FTR) and *Synechocytis sp.* (ssFTR) (PDB ID 1DJ7) showed a high sequence identity of 65 %. Since I could not get the structure of single *At*FTR in non-complexed form, I used ssFTR for the

comparison. The structure of ssFTR and *At*FTR in complex with Trx-*f*2 and Trx-*m*2 were superimposed based on the Cα atoms of FTRC. The superposed model showed no significant structural changes upon complex formation, having the r.m.s.d. value ranging from 0.577 to 0.827 Å (Figure 35a).

The main chain structure of ssFTRC was similar to that of FTRC in FTR:Trx-*f*2 and FTR:Trx-*m*2 except in the N-terminal and C-terminal regions due to their flexibility. However, the structure of ssFTRV was a little bit different especially in loop regions. Therefore, I will focus on the side chain conformation of FTRC at the interface. There were no big conformational changes of FTR upon complex formation, as shown in Figure 35. There were microscopic structural changes by residues R57, Y59, K62, M87, and F96 of FTRC (*A. thaliana* numbering). The intramolecular disulfide was broken between C56 and C86. The residue C56 was flipped to make an intermolecular disulfide bridge with the catalytic redox-active Cys residue of Trx triggering the conformational changes of the neighborhood residues, H58 that also flipped and the residues R57 and Y59. Whereas, the residue C86 made interaction with one iron of the iron-sulfur cluster forming the sulfur-Fe bond as the fifth ligation from Cys and probably affecting the rotation of H85. Notably, the residue H85 in FTR:Trx-*y*1 had a different rotation with H85 in FTR:Trx-*f*2 and FTR:Trx-*m*2.

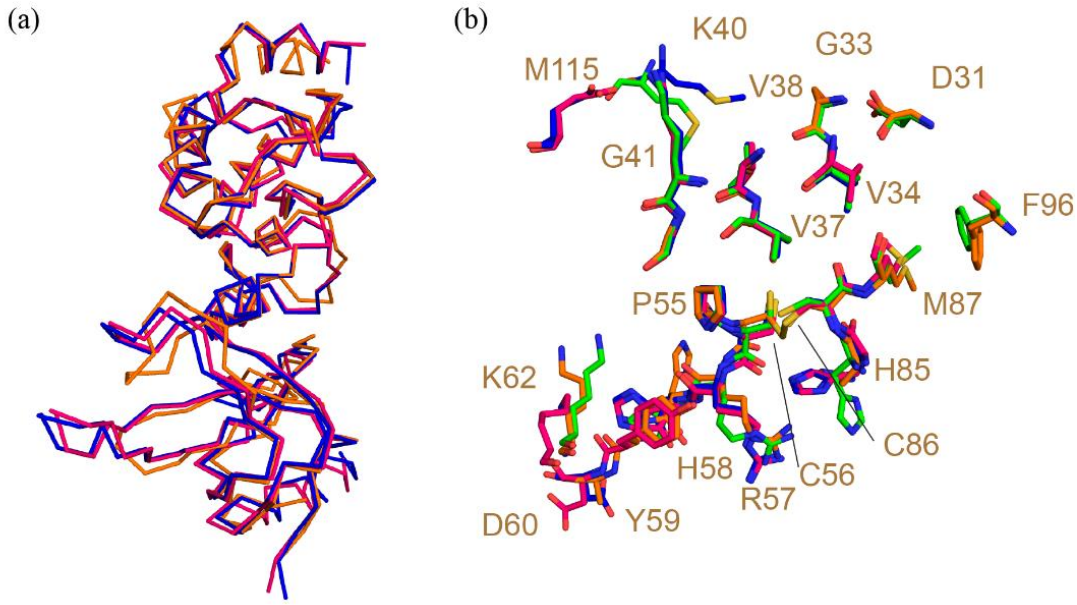

Figure 35 (a). Superposition of ssFTR and atFTR from FTR:Trx-*f*2 and FTR:Trx-*m*2 complex. (b) Side chain of FTRC at the interface shown as a stick model. ssFTR is colored in orange, FTR and the side chain of FTRC from FTR:Trx*f*2 complex in pink, FTR and the side chain of FTRC from FTR:Trx-*m*2 complex in blue and the side chain of FTRC from FTR:Trx-*y*1 in green.

Structural changes of Trx upon complex formation

The sequences identities of Trx-*m*2 and Trx-*m*1 was 81%. Since I cannot make a crystal of Trx-*m*2, the structure of Trx-*m*2 from the complex was superposed with the structure of single Trx-*m*1 using the CCP4 superposition using secondary structure matching of whole chain Trx [46]. The superimposed models are shown in Figure 36 revealing no significant main chain structural change upon complex formation showing the small r.m.s.d. value of 0.670 Å. The overall structure of Trx-*m*2 was similar to that of Trx-

*m*1 except in the N-terminal region. Some residues at the interface displayed minor conformational changes such as K42, D67, R79, and I81 (Trx-*m*2 numbering). Furthermore, W37 and S80 (Trx-*m*2 numbering) were flipped to interact with FTRC through hydrophobic and hydrogen interactions, respectively.

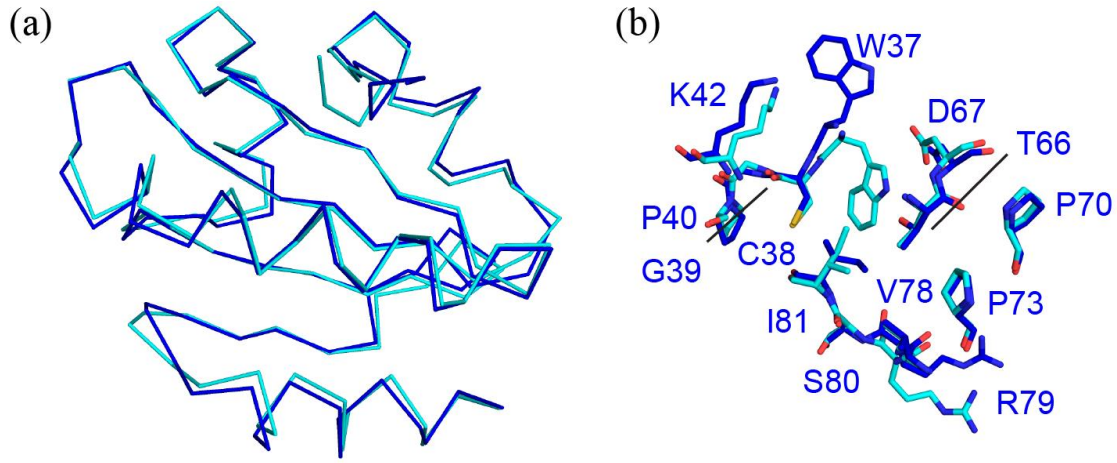

Figure 36 Structural comparison of Trx-*m*2 from FTR:Trx-*m*2 complex and monomer Trx-*m*1 (a). the overall structure and (b). the side chain of the residues which interact with FTRC in the complex shown as a stick model. Trx-*m*2 is colored in blue and Trx-*m*1 in light blue.

The sequence alignment of Trx-*f*2 and spinach Trx-*f* (PDB ID 1FAA) shows high conservation around 75%. I could not get the structure of Trx-*f* monomer from *A.thaliana*. Hence, I will use spinach Trx-*f* as a structured comparison. The overall structure of Trx-*f*2 was similar to that of spinach Trx-*f* with r.m.s.d. of 0.539 Å. The big difference is in the C-terminal region and the conformational changes of the side chain residues at the interface, as shown in Figure 37. The conserved W38 (*A. thaliana* numbering) was flipped which also

happened in Trx-*m*. The residues that display different conformation were K71, I79, R80, V81, and V82 (*A. thaliana* numbering).

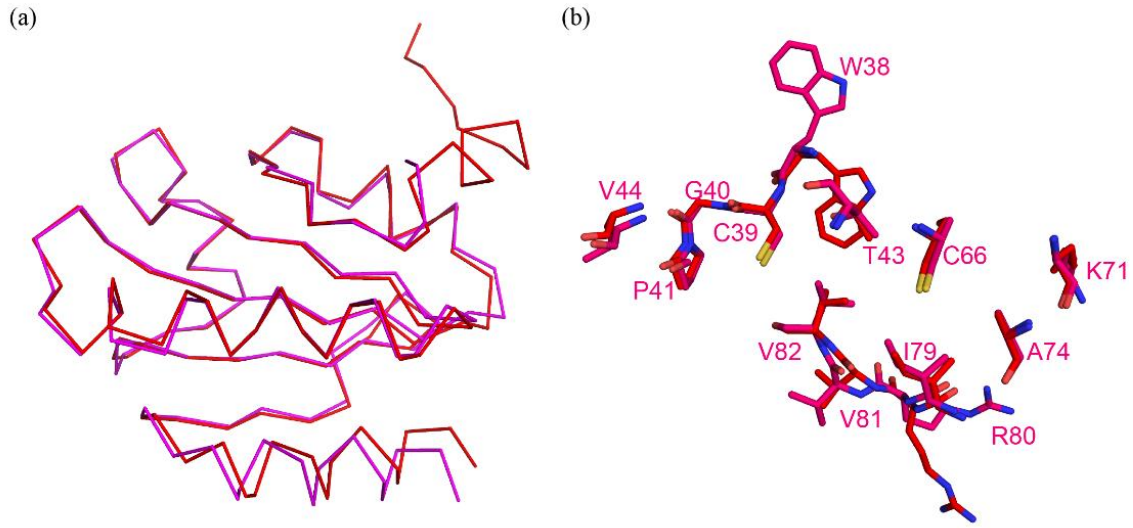

Figure 37 Structural comparison of Trx-*f*2 from FTR:Trx-*f*2 complex and spinach Trx-*f* (a). the overall structure and (b). the side chain of the residues which interact with FTRC in the complex shown as a stick model. Trx-*f*2 is colored in magenta and Trx-*f* in red.

Unfortunately, I could not perform a similar analysis of Trx-*y* because I could not solve the structure of Trx-*y*2 and there is no structure of *y*-type Trx in PDB. I predicted the conformational changes of the conserved tryptophan also occurs in Trx-*y* protein upon complex formation.

CHAPTER 5

COMPARATIVE ANALYSIS OF THE THREE FTR:TRX COMPLEX STRUCTURES

Introduction

In Chapter 1, 2 and 3, I have successfully determined three structures of FTR:Trx protein complex; FTR:Trx-*y*1; FTR:Trx-*f*2; and FTR:Trx-*m*2, at 1.59 Å, 1.79 Å and 2.4 Å, respectively. FTR:Trx-*f*2 and FTR:Trx-*m*2 complexes contained Trx, catalytic and variable subunit of FTR, whereas FTR:Trx-*y*1 contained Trx and FTR catalytic subunit only. The molecular interaction between FTR and Trx from three complexes was similar, but I need to compare the all three structures more quantitatively by the appropriate method. Since the resolution of the complex structures were quite good, I comparatively studied the interaction between FTR and Trxs.

Materials and methods

The superposition of three complexes was performed to check a typical FTR:Trx complex formation and the complex differences. The superposition of three complexes was performed by CCP4 superposition specified residues with fitting Cα atoms of the catalytic subunit of FTR. Figures were prepared using PyMol (The PyMOL Molecular Graphic System, Version 2.0 Schrödinger, LLC), and protein-protein interactions were checked by Dimplot in Ligplot+ [33].

Results

Structural comparison complex protein of FTR with Trx from each group

The superposition of the three complexes, as displayed in Figure 38 reveals that Trx molecules interacted mostly with FTRC and FTR maintained its overall structure with average r.m.s.d. of FTRC was 0.588 Å. The differences were the rotation of Trx molecule perpendicular to the flat of FTR molecule of 7.9-16.1 degrees in the polar angle of kappa and the range r.m.s.d.s of Trx structures was 1.2-1.5 Å. The open β barrel as core Trx molecules was superimposed well whereas the α-helices appear less superimposable.

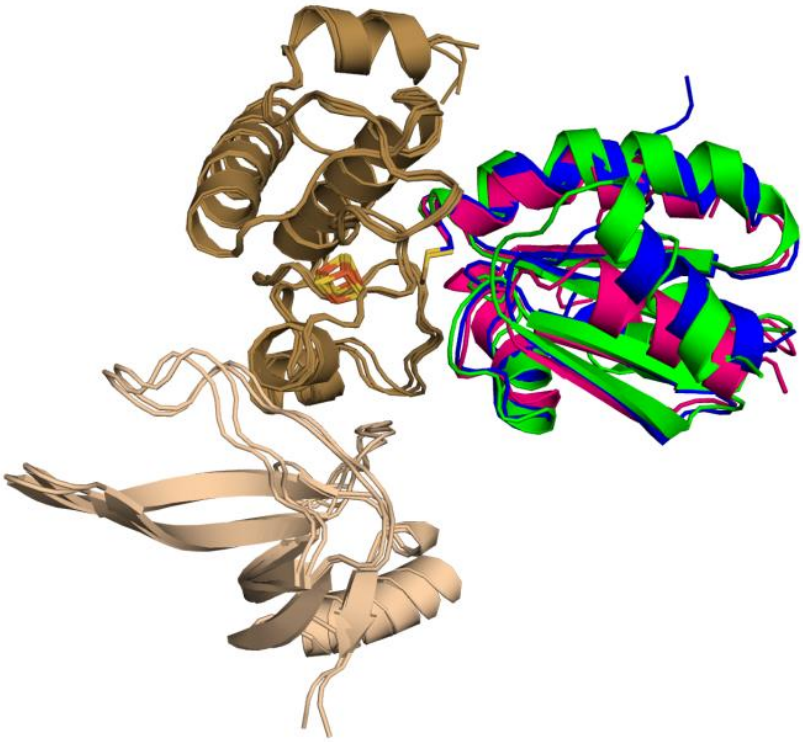

Figure 38 Superposition of three complexes between FTR and three Trx isoforms. The iron-sulfur cluster is shown as a stick model in orange and yellow, the intermolecular disulfide bridge in yellow. FTR is colored in brown, Trx-*y*1 in green, Trx-*f*2 in magenta, and Trx-*m*2 in blue.

Discussion

Structural analysis of the complex between FTR and three isoforms Trx

The genome of *Arabidopsis thaliana* reveals that there are ten isoforms Trx in the chloroplast. On the other hand, the catalytic chain of FTR is encoded by a single gene and the variable chain of FTR is encoded by two genes. Based on the FTR-dependent kinetics, ten Trx isoforms are clustered into three classes: high, middle, and low. The different affinity of FTR to Trx is not fully controlled by the redox potential of Trx [25]. I will discuss the structural basis of differential electron transfer complex formation of FTR to three classes of Trx. The representatives of each class are Trx-*y*1 from the high group, Trx-*f*2 from the middle group, and Trx-*m*2 from the low group.

The interaction between FTR and Trx, shown in Figure 13, Figure 19 and Figure 26, can be distinguished into two types, common interaction and isoform-specific interaction as summarized in Figure 39. The common interaction was conserved among three complexes. The residues of FTRC that made common interactions with Trxs are VXXVVXKG (starting from V34), PCRH (starting from P55), and HC (starting from H85). Interestingly, the interaction of V34 with Trxs can be found in three complexes; however, the interaction partner was different. The residue V34 of FTRC formed hydrophobic interaction with the residues G32 and F36 of Trx-*y*1 in FTR:Trx-*y*1 while it made hydrophobic interaction with V44 of Trx-*f*2 in FTR:Trx-*f*2 and G39 of Trx-*m*2 in FTR:Trx-*m*2. The residues of Trx that formed common interactions with FTRC were located near the active site of Trx protein: the loop connecting the β2 strand and α2 helix and the loop of α3 helix and β4 strand. The interactions at the loop of β2 and α2 had a similar amino acid sequence of WCGP, in contrast to the loop of α3 and β4 that had the variant amino acid

sequences, IEAL for Trx-*y*1 (starting from I71), IRVV for Trx-*f*2 (starting from I79) and VRSI for Trx-*m*2 (starting from V78).

The second category was an isoform-specific interaction that can be found in one or two complexes. The FTR:Trx-*y*1 complex had more isoform-specific interactions than the other two complexes. This was supported by the number of accessible buried surface area between FTRC and Trx which was calculated using ArealMol in the CCP4 program suite [47]. The corresponding area for the FTR:Trx-*y*1 complex was 1622 $Å^2$, whereas the area for FTR:Trx-*f*2 and FTR:Trx-*m*2 was 1470 $Å^2$ and 1509 $Å^2$, respectively. The residues that formed the isoform-specific interactions in FTR:Trx-*y*1 were spread over the peripheral interface of FTR or Trx molecule. On the contrary, the residues that made isoform-specific interactions in FTR:Trx-*f*2 and FTR:Trx-*m*2 were less at the interface (Figure 40). The isoform-specific interactions of each complex may contribute to differentiate the affinity of FTR toward each Trx isoform.

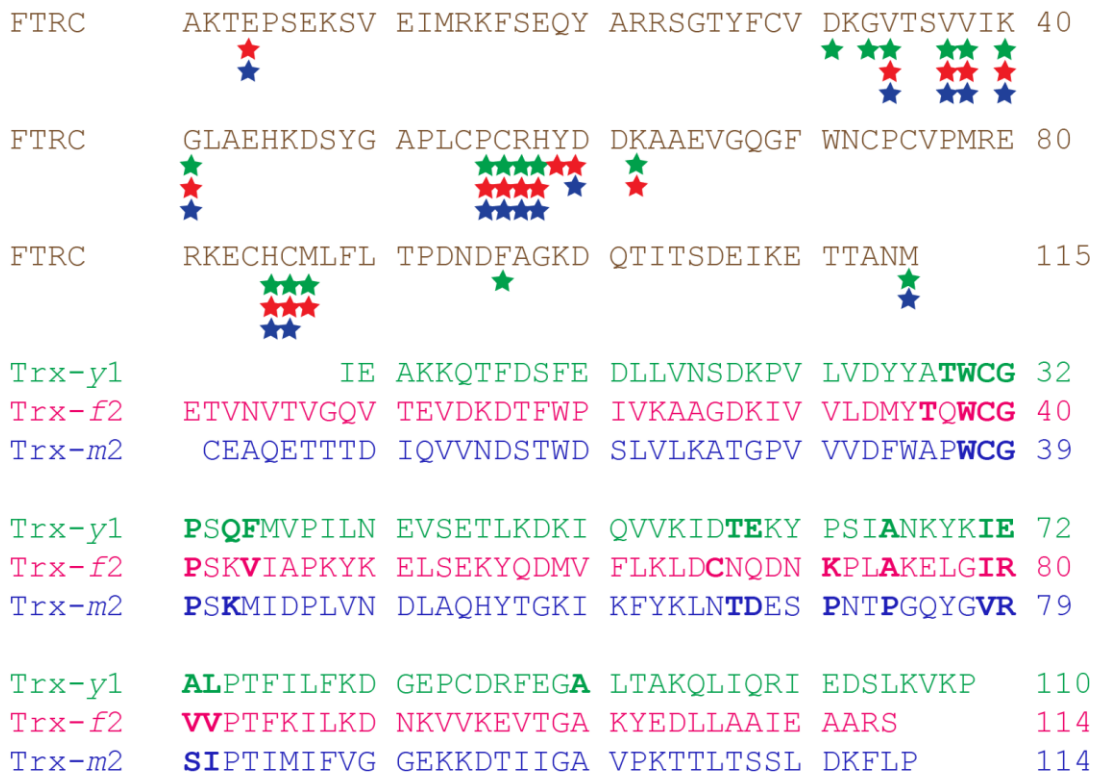

Figure 39 Amino acid sequence alignment of the catalytic subunit of FTR (top) and three isoforms of Trx (bottom). The star and bold characters are shown of interacting residues in the complexes, FTR:Trx-*y*1 in green, FTR:Trx-*f*2 in magenta, and FTR:Trx-*m*2 in blue.

The Trx molecules had a different electrostatic potential at the interface, as shown in Figure 40. The charged surface of Trx-*y*1 at the interface was more negatively charged than that of Trx-*m*2 while the charged surface of Trx-*f*2 at the interface was positively charged. The charged surface of FTR catalytic subunit at the interface was slightly different in each complex adjusting to the differences in the electrostatic potential of Trx interfaces. The charged surface of Trx also may drive the different efficiency of electron transfer activity from FTR to Trxs.

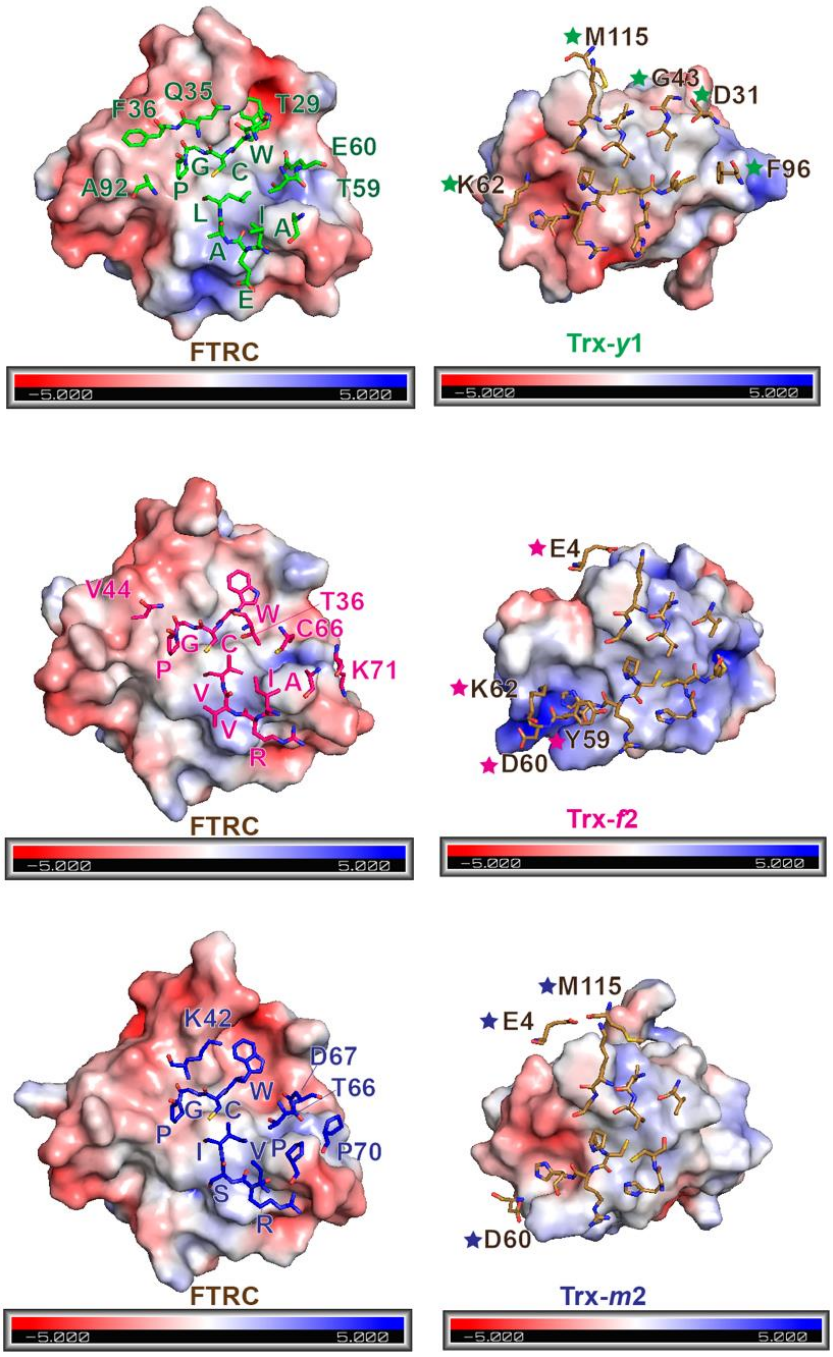

Figure 40 The molecular surfaces of FTR and Trx colored according to the electrostatic potentials are shown in open-book style with interacting residues shown as stick models. A one-letter code with a sequence number corresponds to isoform-specific residues. FTR:Trx-*y*1 in green, FTR:Trx-*f*2 in magenta, and FTR:Trx-*m*2 in blue.

GENERAL DISCUSSION AND CONCLUSION

Plants have evolved multiple adaptive strategies to survive under the fluctuating light environment. For sustainable gain of photosynthetic metabolic flow, chloroplasts have to adjust their biological functions toward varying light conditions. Chloroplasts serve as the site of photosynthesis, and the Fd/Trx system plays a vital role in several chloroplast metabolic pathways. The Fd/Trx system includes Trxs and Trx-like proteins, Fd, FTR and NTR. In plants, the Fd/Trx systems were studied for more than 40 years and suggested to play the central role in regulating malate synthesis during the day and malate consumption during the night [20,48]. The Fd/Trx system studies have expanded and focused on the Calvin Benson cycle, starch synthesis, antioxidant stress resistance and regulations of stress resistance-associated gene [20,49].

The genome of *A. thaliana* encodes 20 Trx isoforms that can be divided into seven subtypes based on amino acid sequence [24,27]. In the chloroplast, ten different Trx isoforms are classified into five subtypes have been reported to be located. Despite the typical structure named Trx-fold, Trxs show different molecular characteristics, such as the electrostatic potential on the molecular surface and midpoint redox potential of the redox active disulfide bond, implying that they display different redox regulatory properties [25,39,50–53]. My collaborators, Dr. Keisuke Yoshida and Prof. Toru Hisabori, studied on FTR-dependent kinetics parameters of Trxs. Trxs showed different efficiencies: high, middle and low, as displayed in Figure 5. It should be noted that it was not dependent on redox potential. It may be caused by other factors such as the electrostatic potentials on the molecular surface of Trx and the resulting protein-protein interaction. The complex structures between *synechocystis* FTR and two Trx isoform (Trx-*f* and -*m*) from spinach

have been solved by Dai *et al.* (2007). The structures reveal that Trx molecules interact exclusively with the catalytic subunit of FTR and there are no significant differences. These could not explain three types of different efficiencies of *A. thaliana* FTR to Trxs.

Therefore, I tried to determine the complex structure between FTR and three representatives of Trx from *A. thaliana* representing each class to study the structural basis of the different efficiency of FTR activity toward Trx. I have selected Trx-*y*1 from the high group, Trx-*f*2 from the middle group and Trx-*m*2 from the low group. The mutation of buried active site Cys to Ser of Trx allows stabilizing the intermolecular disulfide bridge between FTR and Trx. Using this approach, I made FTR:Trx complex by mixing the wild type FTR with mutant Trx in the presence of DTT. The complex was purified by cation and anion exchange chromatography which improve the sample purity for crystallization.

In Chapter 1, the crystal structure of FTR:Trx-*y*1 was solved at 1.59 Å resolution. It contained Trx-*y*1 and only catalytic subunit of FTR. The variable subunit was lost unexpectedly during crystallization process which was confirmed by SDS-PAGE in Figure 11. The crystal packing could explain this phenomenon. There were two interfaces of FTRC with Trx-*y*1 and crystallography symmetry mate Trx-y1 (Trx-*y*1') (Figure 10). The latter was supposed to be the interface of FTRC with FTRV. The residues E80 and R81 of FTRC interacted with D13 of Trx-*y*1'. It should be noted that E80 and R81 play an important role in the interaction between FTR subunits. Moreover, the residue D13 is unique to Trx-*y* which is substituted by I21 and S20 in Trx-*f*2 and Trx-*m*2 sequences, respectively. This explained why the variable subunit was lost in only FTR:Trx-*y*1 complex but no other two complexes. The crystallization condition of FTR:Trx-*y*1 may weaken the interaction of FTR subunits and accelerate the interaction of FTRC with Trx-*y*1'.

In Chapter 2 and 3, I have determined the structure of FTR:Trx-*f*2 and FTR:Trx-*m*2 complexes. The obtained structure of FTR:Trx-*f*2 was similar to that of FTR:Trx-*m*2. Trx molecules interact mostly with FTRC. Trx made interaction with FTRV through hydrophobic interaction by residue S77 of FTRV and R80 of Trx-*f*2 (R79 of Trx-*m*2). The structural comparison of FTR:Trx-*y*1, FTR:Trx-*f*2 and FTR:Trx-*m*2 showed no significant differences except in the rotation of Trx molecule perpendicular to FTR molecule of 7.9-16.1 degrees in the polar angle of kappa (Figure 38). The r.m.s.d. of FTRC ranged from 0.52-0.74 Å. I'd like to note that the first structure of FTR from the higher plant had been determined in the complex form in this research. The catalytic subunit of FTR was similar to *Synechocystis* FTR. In contrast, the variable subunit was a little bit different due to less conserved of the sequence. Residues 1 to 23 in the N-terminal region of FTRV were invisible. It may be caused by flexibility or cleavage because those N-terminal regions are rich with serine residues, implying its structural instability [40]. In the spinach FTR case, the removal of up to 24 N-terminal residues of the variable subunit stabilizes FTR and does not change any catalytic properties [41].

In Chapter 4, I have discussed about the structural difference upon complex formation. In order to study the structural changes upon complex formation, I used the structure of ssFTR (PDB ID 1DJ7) as a reference of FTR to compare the structure of FTR in the complex form, Trx-*m*1 as a reference of Trx-*m*2 in the complex form and spinach Trx-*f* (PDB ID 1FAA) as a reference of Trx-*f*2 in the complex form. The structure comparison of the FTR or Trx in single form and complex form showed that there were microscopic structural changes of FTR or Trx upon complex formation. The r.m.s.d. of FTRC was ranging from 0.577 to 0.827 Å, and the r.m.s.d. of Trx-*m* and Trx-*f* was 0.670

and 0.539 Å, respectively. The significant differences were caused by changes in the side chain conformations at the interface that was used for fine-tuning of FTR interaction with Trx isoforms, leading to different affinity of FTR toward Trx isoforms

In Chapter 5, I have compared the three obtained FTR:Trx structures to discuss about the isoform-specific molecular interaction. The interaction between FTR and Trxs, shown in Figure 39, can be distinguished into two types, common interaction among all three FTR:Trx complexes and the isoform-specific interactions. Notably, the common interaction by residue V34 of FTRC with Trxs could be found in three complexes; however, the interaction partner was different. The FTR:Trx-*y*1 complex had more interaction than the other two complexes. It was supported by the total buried accessible area. The corresponding area for the FTR:Trx-*y*1 complex was 1622 $Å^2$, whereas the area for FTR:Trx-*f*2 and FTR:Trx-*m*2 was 1470 $Å^2$ and 1509 $Å^2$, respectively. Furthermore, Trx molecules displayed the different electrostatic potentials mapped on the molecular surfaces, which influenced the subtle structural changes of FTRC at the interface. The isoform-specific interaction located peripherally at the intermolecular interface and the obvious differences in the electrostatic potentials at the molecular surface of Trx may be the primary driver of the isoform-specific electron transfer efficiency from FTR to Trxs.

REFERENCES

[1] M.P. Johnson, Photosynthesis, Essays Biochem. 60 (2016) 255–273. https://doi.org/10.1042/EBC20160016.

[2] L. Michelet, M. Zaffagnini, S. Morisse, F. Sparla, M.E. Pérez-Pérez, F. Francia, A. Danon, C.H. Marchand, S. Fermani, P. Trost, S.D. Lemaire, Redox regulation of the Calvin-Benson cycle: Something old, something new, Front. Plant Sci. 4 (2013) 1–21. https://doi.org/10.3389/fpls.2013.00470.

[3] C. Spetea, E. Rintamäki, B. Schoefs, Changing the light environment: Chloroplast signalling and response mechanisms, Philos. Trans. R. Soc. B Biol. Sci. 369 (2014) 1–3. https://doi.org/10.1098/rstb.2013.0220.

[4] R.M. Larkin, Influence of plastids on light signalling and development, Philos. Trans. R. Soc. B Biol. Sci. 369 (2014). https://doi.org/10.1098/rstb.2013.0232.

[5] B.C. Tripathy, R. Oelmüller, Reactive oxygen species generation and signaling in plants, Plant Signal. Behav. 7 (2012) 1621–1633. https://doi.org/10.4161/psb.22455.

[6] H. Kirchhoff, Chloroplast ultrastructure in plants, New Phytol. 223 (2019) 565–574. https://doi.org/10.1111/nph.15730.

[7] L. Vogelsang, K.J. Dietz, Regulatory thiol oxidation in chloroplast metabolism, oxidative stress response and environmental signaling in plants, Biochem. J. 477 (2020) 1865–1878. https://doi.org/10.1042/BCJ20190124.

[8] G. Noctor, J.P. Reichheld, C.H. Foyer, ROS-related redox regulation and signaling in plants, Semin. Cell Dev. Biol. 80 (2018) 3–12. https://doi.org/10.1016/j.semcdb.2017.07.013.

[9] K.J. Dietz, Redox signal integration: From stimulus to networks and genes, Physiol. Plant. 133 (2008) 459–468. https://doi.org/10.1111/j.1399-3054.2008.01120.x.

[10] P. Schürmann, R.A. Wolosiuk, Studies on the regulatory properties of chloroplast fructose-1,6-bisphosphatase, Biochim. Biophys. Acta. 522 (1978) 130–138.

[11] C. Queiroz-Claret, J.C. Meunier, Light Activation of Sedoheptulose-1,7-Bisphosphatase by aReconstituted Thylakoid System Compared with DTT Activation. Evidence for Protein-Enzyme Interactions, J. Plant Physiol. 145 (1995) 45–49. https://doi.org/10.1016/S0176-1617(11)81844-4.

[12] B.B. Buchanan, Role of Light in the Regulation of Chloroplast Enzymes, Annu. Rev. Plant Physiol. 31 (1980) 341–374. https://doi.org/10.1146/annurev.pp.31.060180.002013.

[13] K. Yoshida, Y. Yokochi, T. Hisabori, New Light on Chloroplast Redox Regulation: Molecular Mechanism of Protein Thiol Oxidation, Front. Plant Sci. 10 (2019) 1–6. https://doi.org/10.3389/fpls.2019.01534.

[14] K.J. Dietz, R. Hell, Thiol switches in redox regulation of chloroplasts: Balancing redox state, metabolism and oxidative stress, Biol. Chem. 396 (2015) 483–494. https://doi.org/10.1515/hsz-2014-0281.

[15] K. Yoshida, T. Hisabori, Two distinct redox cascades cooperatively regulate chloroplast functions and sustain plant viability, Proc. Natl. Acad. Sci. U. S. A. 113 (2016) E3967–E3976. https://doi.org/10.1073/pnas.1604101113.

[16] S. Dai, C. Schwendtmayer, P. Schürmann, S. Ramaswamy, H. Eklund, Redox signaling in chloroplasts: Cleavage of disulfides by an iron- sulfur cluster, Science (80-.). 287 (2000) 655–658. https://doi.org/10.1126/science.287.5453.655.

[17] E. Keryer, V. Collin, D. Lavergne, S. Lemaire, E. Issakidis-Bourguet, Characterization of Arabidopsis mutants for the variable subunit of ferredoxin:thioredoxin reductase, Photosynth. Res. 79 (2004) 265–274. https://doi.org/10.1023/B:PRES.0000017173.46185.3e.

[18] E. Gelhaye, N. Rouhier, N. Navrot, J.P. Jacquot, The plant thioredoxin system, Cell. Mol. Life Sci. 62 (2005) 24–35. https://doi.org/10.1007/s00018-004-4296-4.

[19] F.J. Cejudo, A.J. Meyer, J.P. Reichheld, N. Rouhier, J.A. Traverso, Thiol-based redox homeostasis and signaling, Front. Plant Sci. 5 (2014) 2013–2015. https://doi.org/10.3389/fpls.2014.00266.

[20] Y. Meyer, J.P. Reichheld, F. Vignols, Thioredoxins in Arabidopsis and other plants, Photosynth. Res. 86 (2005) 419–433. https://doi.org/10.1007/s11120-005-5220-y.

[21] G. Capitani, Z. Marković-Housley, G. DelVal, M. Morris, J.N. Jansonius, P. Schürmann, Crystal structures of two functionally different thioredoxins in spinach chloroplasts, J. Mol. Biol. 302 (2000) 135–154. https://doi.org/10.1006/jmbi.2000.4006.

[22] J.L. Martin, Thioredoxin -a fold for all reasons, Structure. 3 (1995) 245–250. https://doi.org/10.1016/S0969-2126(01)00154-X.

[23] S. Dai, R. Friemann, D.A. Glauser, F. Bourquin, W. Manieri, P. Schürmann, H. Eklund, Structural snapshots along the reaction pathway of ferredoxin-thioredoxin reductase, Nature. 448 (2007) 92–96. https://doi.org/10.1038/nature05937.

[24] The Arabidopsis Genome Initiative, Analysis of the genome sequence of the flowering plant Arabidopsis thaliana, Nature. 408 (2000) 796–815. https://doi.org/10.1038/35048692.

[25] K. Yoshida, T. Hisabori, Distinct electron transfer from ferredoxin-thioredoxin reductase to multiple thioredoxin isoforms in chloroplasts, Biochem. J. 474 (2017) 1347–1360. https://doi.org/10.1042/BCJ20161089.

[26] K. Chibani, L. Tarrago, P. Schürmann, J.P. Jacquot, N. Rouhier, Biochemical properties of poplar thioredoxin z, FEBS Lett. 585 (2011) 1077–1081. https://doi.org/10.1016/j.febslet.2011.03.006.

[27] Y. Meyer, F. Vignols, J.P. Reichheld, Classification of plant thioredoxins by sequence similarity and intron position, Methods Enzymol. 347 (2002) 394–402. https://doi.org/10.1016/S0076-6879(02)47039-5.

[28] V. Collin, P. Lamkemeyer, M. Miginiac-Maslow, M. Hirasawa, D.B. Knaff, K.J. Dietz, E. Issakidis-Bourguet, Characterization of plastidial thioredoxins from arabidopsis belonging to the new y-type, Plant Physiol. 136 (2004) 4088–4095. https://doi.org/10.1104/pp.104.052233.

[29] L. Nikkanen, E. Rintamäki, Thioredoxin-dependent regulatory networks in chloroplasts under fluctuating light conditions, Philos. Trans. R. Soc. B Biol. Sci. 369 (2014) 1–7. https://doi.org/10.1098/rstb.2013.0224.

[30] W. Kabsch, XDS, Acta Crystallogr. Sect. D Biol. Crystallogr. 66 (2010) 125–132. https://doi.org/10.1107/S0907444909047337.

[31] A.J. McCoy, R.W. Grosse-Kunstleve, P.D. Adams, M.D. Winn, L.C. Storoni, R.J. Read, Phaser crystallographic software, J. Appl. Crystallogr. 40 (2007) 658–674. https://doi.org/10.1107/S0021889807021206.

[32] D. Liebschner, P. V. Afonine, M.L. Baker, G. Bunkoczi, V.B. Chen, T.I. Croll, B. Hintze, L.W. Hung, S. Jain, A.J. McCoy, N.W. Moriarty, R.D. Oeffner, B.K. Poon, M.G. Prisant, R.J. Read, J.S. Richardson, D.C. Richardson, M.D. Sammito, O. V. Sobolev, D.H. Stockwell, T.C. Terwilliger, A.G. Urzhumtsev, L.L. Videau, C.J. Williams, P.D. Adams, Macromolecular structure determination using X-rays, neutrons and electrons: Recent developments in Phenix, Acta Crystallogr. Sect. D Struct. Biol. 75 (2019) 861–877. https://doi.org/10.1107/S2059798319011471.

[33] R.A. Laskowski, M.B. Swindells, LigPlot+: multiple ligand-protein interaction diagrams for drug discovery, J. Chem. Inf. Model. 51 (2011) 2778–2786.

[34] B.W. Matthews, Solvent content of protein crystals, J. Mol. Biol. 33 (1968) 491–497. https://doi.org/10.1016/0022-2836(68)90205-2.

[35] A.J. McCoy, Acknowledging errors: Advanced molecular replacement with phaser, Methods Mol. Biol. 1607 (2017) 421–453. https://doi.org/10.1007/978-1-4939-7000-1_18.

[36] P. Emsley, B. Lohkamp, W.G. Scott, K. Cowtan, Features and development of Coot, Acta Crystallogr. Sect. D Biol. Crystallogr. 66 (2010) 486–501. https://doi.org/10.1107/S0907444910007493.

[37] P. V. Afonine, R.W. Grosse-Kunstleve, N. Echols, J.J. Headd, N.W. Moriarty, M. Mustyakimov, T.C. Terwilliger, A. Urzhumtsev, P.H. Zwart, P.D. Adams, Towards automated crystallographic structure refinement with phenix.refine, Acta Crystallogr. Sect. D Biol. Crystallogr. 68 (2012) 352–367. https://doi.org/10.1107/S0907444912001308.

[38] S. Dai, C. Schwendtmayer, K. Johansson, S. Ramaswamy, P. Schürmann, H. Eklund, How does light regulate chloroplast enzymes? Structure-function studies of the ferredoxin/thioredoxin system, Q. Rev. Biophys. 33 (2000) 67–108. https://doi.org/10.1017/S0033583500003607.

[39] K. Yoshida, S. Hara, T. Hisabori, Thioredoxin selectivity for thiol-based redox regulation of target Proteins in Chloroplasts, J. Biol. Chem. 290 (2015) 14278–14288. https://doi.org/10.1074/jbc.M115.647545.

[40] E. Gaymard, L. Franchini, W. Manieri, E. Stutz, P. Schürmann, A dicistronic construct for the expression of functional spinach chloroplast ferredoxin: Thioredoxin reductase in Escherichia coli, Plant Sci. 158 (2000) 107–113. https://doi.org/10.1016/S0168-9452(00)00310-1.

[41] W. Manieri, L. Franchini, L. Raeber, S. Dai, A.L. Stritt-Etter, P. Schürmann, N-terminal truncation of the variable subunit stabilizes spinach ferredoxin:Thioredoxin reductase, FEBS Lett. 549 (2003) 167–170. https://doi.org/10.1016/S0014-5793(03)00811-1.

[42] P. Wang, J. Liu, B. Liu, D. Feng, Q. Da, P. Wang, S. Shu, J. Su, Y. Zhang, J. Wang, H. Bin Wang, Evidence for a role of chloroplastic m-type thioredoxins in the biogenesis of photosystem II in arabidopsis, Plant Physiol. 163 (2013) 1710–1728. https://doi.org/10.1104/pp.113.228353.

[43] Z. Kang, T. Qin, Z. Zhao, Thioredoxins and thioredoxin reductase in chloroplasts: A review, Gene. 706 (2019) 32–42. https://doi.org/10.1016/j.gene.2019.04.041.

[44] M.D. Winn, C.C. Ballard, K.D. Cowtan, E.J. Dodson, P. Emsley, P.R. Evans, R.M. Keegan, E.B. Krissinel, A.G.W. Leslie, A. McCoy, S.J. McNicholas, G.N. Murshudov, N.S. Pannu, E.A. Potterton, H.R. Powell, R.J. Read, A. Vagin, K.S. Wilson, Overview of the CCP4 suite and current developments, Acta Crystallogr. Sect. D Biol. Crystallogr. 67 (2011) 235–242. https://doi.org/10.1107/S0907444910045749.

[45] G.M. Sheldrick, Crystal structure refinement with SHELXL, Acta Crystallogr. Sect. C Struct. Chem. 71 (2015) 3–8. https://doi.org/10.1107/S2053229614024218.

[46] E. Krissinel, K. Henrick, Secondary-structure matching (SSM), a new tool for fast protein structure alignment in three dimensions, Acta Crystallogr. Sect. D Biol. Crystallogr. 60 (2004) 2256–2268. https://doi.org/10.1107/S0907444904026460.

[47] B. Lee, F.M. Richards, The interpretation of protein structures: Estimation of static accessibility, J. Mol. Biol. 55 (1971). https://doi.org/10.1016/0022-2836(71)90324-X.

[48] B.B. Buchanan, R.A. Wolosiuk, P. Schürmann, Thioredoxin and enzyme regulation, Trends Biochem. Sci. 4 (1979) 93–96. https://doi.org/10.1016/0968-0004(79)90191-9.

[49] Z. Kang, T. Qin, Z. Zhao, Thioredoxins and thioredoxin reductase in chloroplasts: A review, Gene. 706 (2019) 32–42. https://doi.org/10.1016/j.gene.2019.04.041.

[50] S.K. Katti, D.M. LeMaster, H. Eklund, Crystal structure of thioredoxin from Escherichia coli at 1.68 Å resolution, J. Mol. Biol. 212 (1990) 167–184. https://doi.org/10.1016/0022-2836(90)90313-B.

[51] A. Weichsel, J.R. Gasdaska, G. Powis, W.R. Montfort, Crystal structures of reduced, oxidized, and mutated human thioredoxins: Evidence for a regulatory homodimer, Structure. 4 (1996) 735–751. https://doi.org/10.1016/S0969-2126(96)00079-2.

[52] S.D. Lemaire, M. Miginiac-Maslow, The thioredoxin superfamily in Chlamydomonas reinhardtii, Photosynth. Res. 82 (2004) 203–220. https://doi.org/10.1007/s11120-004-1091-x.

[53] S.D. Lemaire, D. Tedesco, P. Crozet, L. Michelet, S. Fermani, M. Zaffagnini, J. Henri, Crystal structure of chloroplastic thioredoxin f2 from Chlamydomonas reinhardtii reveals distinct surface properties, Antioxidants. 7 (2018). https://doi.org/10.3390/antiox7120171.

LIST OF PUBLICATION

Juniar, L., Tanaka, H., Yoshida, K., Hisabori, T., and Kurisu, G. Structural basis for Thioredoxin isoform-based fine tuning of Ferredoxin-Thioredoxin Reductase activity (2020). Protein Science. (in press)
First published: 04 October 2020 https://doi.org/10.1002/pro.3964